Supporting information:

Enhancing the electrocatalytic activity and stability of Prussian blue analogues by increasing their electroactive sites through the introduction of Au nanoparticles

Roger Sanchis-Gual,[a] Toribio F. Otero,[b] Marc Coronado-Puchau,[a]* Eugenio Coronado[a]*

a. Instituto de Ciencia Molecular, Universitat de València, Catedrático José Beltran 2, 46980, Paterna, Spain

b. Centre for Electrochemistry and Intelligent Materials (CEMI), Universidad Politécnica de Cartagena, Aulario II, Paseo Alfonso XIII, E-30203 Cartagena, Murcia, Spain

Experimental Section

Materials:

All chemical reagents were purchased and used without further purification. Potassium ferricyanide, gold (I) potassium cyanide, nickel (II) chloride hexahydrate, cobalt (II) chloride hexahydrate, potassium borohydride, Chloroauric acid, sodium citrate tribasic dehydrate, thiol polyethylene glycol amine (HS-PEG$_{3.5K}$-NH$_2$), potassium hydroxide (99.99%) and Nafion (117 solution) were purchased from Sigma-Aldrich. Carbon black, acetylene 50% compressed, was obtained from Alfa Aesar (99.9%). Milli-Q water was obtained from a Millipore Milli-Q equipment.

Nanoparticles synthesis

To prepare Au@NiFe NPs, 0.20 mmol of potassium borohydride (KBH$_4$) was added to 100 mL of an aqueous 0.5 mM solution of K[Au(CN)$_2$] under vigorous stirring at around 10 ºC. After 20-30 min, aqueous solutions of K$_3$[Fe(CN)$_6$] (5.7 mM) and NiCl$_2$·6H$_2$O (5.0 mM) were added simultaneously at a rate of 2 mL·h^{-1} to the Au NPs solution under vigorous stirring. After completion of the addition, the solution was vigorously stirred for half an hour. In order to prepare Au@CoFe NPs, 0.20 mmol of KBH$_4$ was added to 100 mL of an aqueous 0.5 mM solution of K[Au(CN)$_2$] under vigorous stirring at around 10 ºC. 10-15 minutes after the solution turns red, aqueous solutions of K$_3$[Fe(CN)$_6$] (5.7 mM) and CoCl$_2$·6H$_2$O (5.0 mM) were added simultaneously at an addition rate of 0.5 mL·h^{-1} to the Au NPs solution under vigorous stirring. After completion of the addition, the solution was vigorously stirred for half an hour. Core@shell NPs were washed with water (11000 rpm for 20 minutes) and finally were dried under vacuum. A thinner and a thicker shell were achieved by adding respectively 2 and 10 mL of each precursor solution. The very thick shell of NiFe was achieved by adding 15 mL of each precursor. K[Au(CN)$_2$] reduction was carried out in an ice bath in order to produce smaller Au cores.

PBA-NiFe NPs of around 150 nm were synthesized at room temperature by adding simultaneously, to 100 mL aqueous solution at 2 mL·h^{-1} rate, aqueous solutions of CoCl$_2$·6H$_2$O (5.0 mM, 7 mL) and K$_3$[Fe(CN)$_6$] (5.7 mM, 7 mL). PBA-CoFe NPs of around 180 nm were also synthesized at room temperature by adding, to 100 mL aqueous solution at 2 mL·h^{-1} rate, aqueous solutions of NiCl$_2$·6H$_2$O (5.0 mM, 8 mL) and K$_3$[Fe(CN)$_6$] (5.7 mM, 8 mL). After completion of the addition, the mixtures were stirred for half an hour before being centrifuged at 11000 rpm for 20 min. The supernatants were removed, and the powders were let dried under vacuum. PBA-NiFe^{II} and PBA-CoFe^{II} were prepared using the same synthetic procedure but adding 0.4 mmol of potassium borohydride (KBH$_4$) to promote the reduction of Fe^{III}.

Au NPs stabilized by citrate capping agent were synthesized following the well-known Turkevich method.[1] Physical mixture (Au+PBA) was prepared by joining in weight 30 % of Au NPs and 70 % of PBA NPs.

The decoration of Au on PBA NPs was carried out by connecting each NP by a polymer containing a thiol and an amine group(HS-PEG-NH$_2$) following a protocol developed in our group.[2]

Electrode preparation

For the electrode preparation, a dispersion composed of 1 mg of powder material, 0.5 mg of acetylene black, 200 µL of water and ethanol (1:1) and 8 µL of Nafion (10 %) was sonicated in order to obtain a well-dispersed suspension. Then, 3.6 µL was drop-casted in a previously polished (sequentially with 1.0, 0.3 and 0.05 µm alumina powder) 3 mm Glassy Carbon electrode. Afterwards, the solvent was let evaporated at room temperature. The electrode mass loading achieved was around 0.25 mg·cm^{-2}.

Electrochemical measurements

Electrochemical tests were performed in a three-electrode cell equipped with Glassy Carbon acting as the working electrode and a platinum wire as the counter electrode. As the reference electrode, a silver-silver chloride (Ag/AgCl (3 M KCl)) was used. All potentials were converted referring to the oxygen evolution overpotential or the reversible hydrogen electrode (RHE). The measurements were performed at least three times for every sample using different electrodes on an Autolab PGSTAT 128N potentiostat/galvanostat. Linear sweep voltammetry (LSV) measurements were carried out at 5 mV·s^{-1} in a previously N$_2$ purged 1 M KOH aqueous solution. Prior to this, cyclic voltammetries (CVs) were performed at different scan rates (100, 50, 20 and 10 mV·s^{-1}). LSV experiments were also carried out in an acidic solution (0.5 M H$_2$SO$_4$) using the same three-electrode cell and electrodes.

Electrochemical surface area (ECSA) was acquired by measuring the current associated with double-layer capacitance from the scan rate dependence of CVs. The potential range used for the CVs was from -0.2 to 0.1 V versus Ag/AgCl (3 M KCl). The scan rates were 400, 300, 200, 100 and 50 mVs^{-1}. The double layer capacitance was estimated by plotting the (ja–jc) (anodic versus cathodic currents) at -0.05 V versus Ag/AgCl (3 M KCl) against the scan rate. The ECSA was measured on the working electrodes after performing an activation process consisting of 5 CVs at 50 mV·s^{-1} around their redox processes.

The turnover frequency (TOF) values were calculated from the following equation:

$$TOF = \frac{jA}{4Fn}$$

where j is the current density at a given overpotential of 0.35 V, A is the surface area of the working electrode, F is the Faraday constant, and n is the total number of moles of PBA or the elctroactive number of moles of PBA.

Electrochemical impedance spectroscopy (EIS) measurements were carried out using a Gamry 1000E potentiostat/galvanostat controlled by Gamry software by applying an AC amplitude of 10 mV in the frequency range of 10^{-1}–10^5 Hz at an overpotential of 0.4 V. EIS data were analyzed and fitted by means of Gamry Echem Analyst v. 7.07 software.

Stability tests were performed under a constant current density of 20 mA·cm^{-2} during 24 h using Ni foam foil (which area is 0.6 cm^2) as the working electrode containing 0.25 mg·cm^{-2} of electrocatalyst mass.

Physical characterization

UV/Vis Spectroscopy: UV-vis absorption spectra were recorded on a Jasco V-670 spectrophotometer in baseline mode from 300 to 900 nm range, using 1.000-cm-optical-path plastic cuvettes.

Attenuated total reflectance Fourier-transform infrared (ATR-FTIR): spectra were collected in an Agilent Cary 630 FTIR spectrometer in the 4000–500 cm−1 range in absence of KBr pellets.

Inductively Coupled-Plasma Mass Spectrometry (ICP-MS): The ICP-MS analysis were conducted at the Universidad de Valencia (Sección de Espectrometría Atómica y Molecular). Samples were digested in an acid medium at 220 ºC using a microwave oven.

Transmission Electron Microscopy (TEM): TEM studies were carried out on a JEOL JEM 1010 microscope operating at 100 kV, and Technai G2 F20 microscope operating at 200 kV. Samples were prepared by dropping suspensions on lacey formvar/carbon copper grids (300 mesh).

Magnetic Measurements: Magnetic data were collected with a Quantum Design MPMS XL-5 susceptometer equipped with a SQUID sensor. Field Cooling magnetization measurements were performed under a magnetic field applied of 1000 Oe.

Raman Spectroscopy: Raman spectra were acquired with a Raman Emission Horiba-MTB Xplora Spectrometer in ambient conditions. NPs were measured with a laser wavelength of 532 nm by drop-casting the samples onto silicon substrates.

Powder X-Ray Diffraction (PXRD): PXRD patterns were obtained with a PANalytical X'Pert diffractometer using the copper radiation (Cu-Ka = 1.54178 Å) in the 5–50 region.

X-ray Photoelectron Spectroscopy (XPS): Samples were analyzed using a K-ALPHA Thermo Scientific spectrometer. All spectra were collected using Al Kα radiation (1486.6 eV), monochromatized by a twin crystal monochromator, yielding a focused X-ray spot (elliptical in shape with a major axis length of 400 μm) at 30 mA and 2 kV. The alpha hemispherical analyzer was operated in the constant energy mode with survey scan pass energies of 200 eV to measure the whole energy band and 50 eV in a narrow scan to selectively measure the particular elements. XPS data were analyzed with Avantage software. A smart background function was used to approximate the experimental backgrounds. Charge compensation was achieved with the system flood gun that provides low energy electrons and low energy argon ions from a single source.
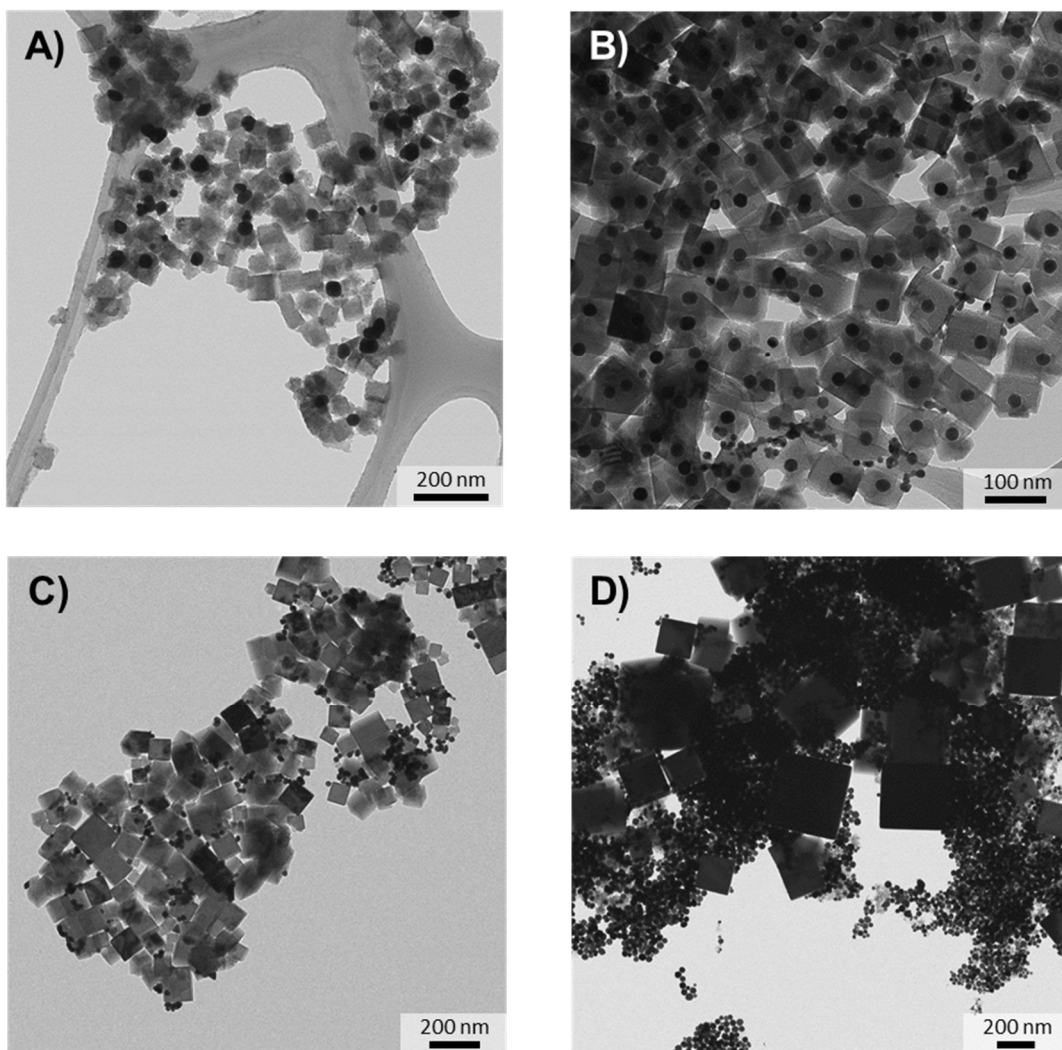
Figure S1. TEM images of the NPs obtained through the Au@CoFe protocol and applying the following parameters: A) addition rate of 2 mL·h⁻¹ and time delay of 20-30 min. B) addition rate of 0.5 mL·h⁻¹ and time delay of 20-30 min. C) addition rate of 0.5 mL·h⁻¹ and time delay of 45 min. D) addition rate of 0.5 mL·h⁻¹ and time delay of 0 min.
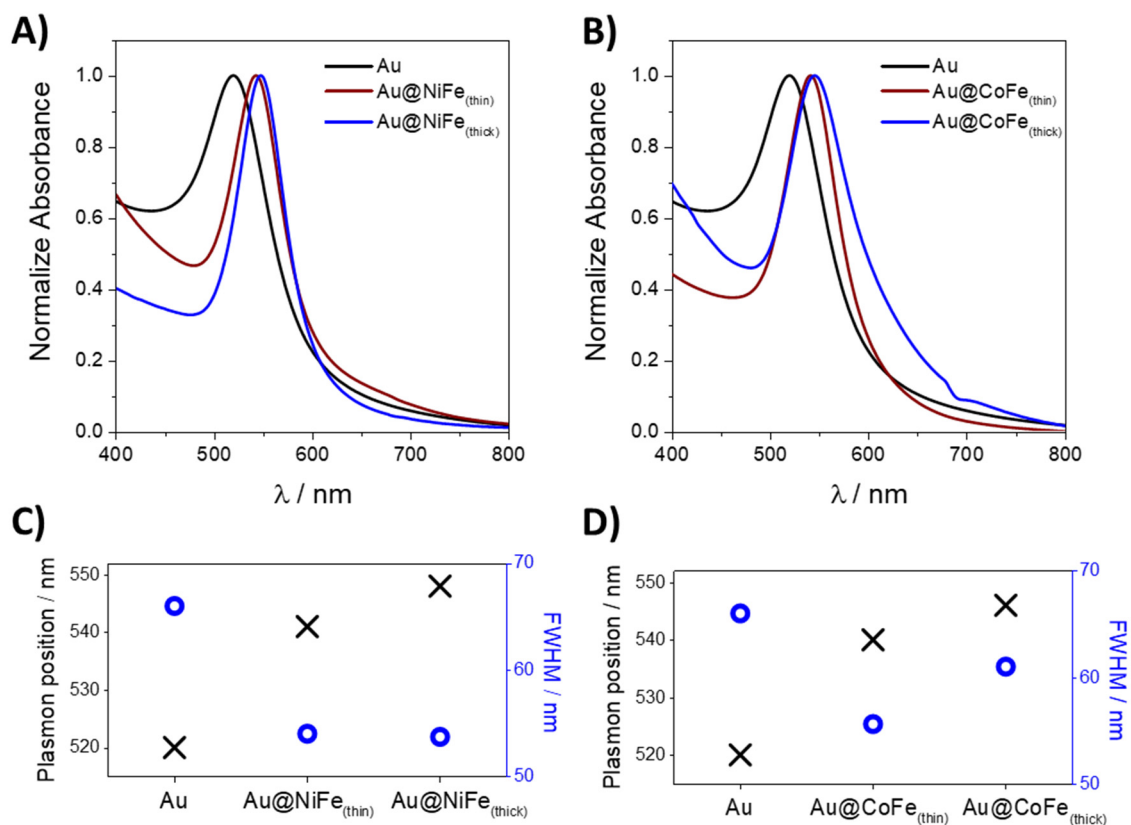
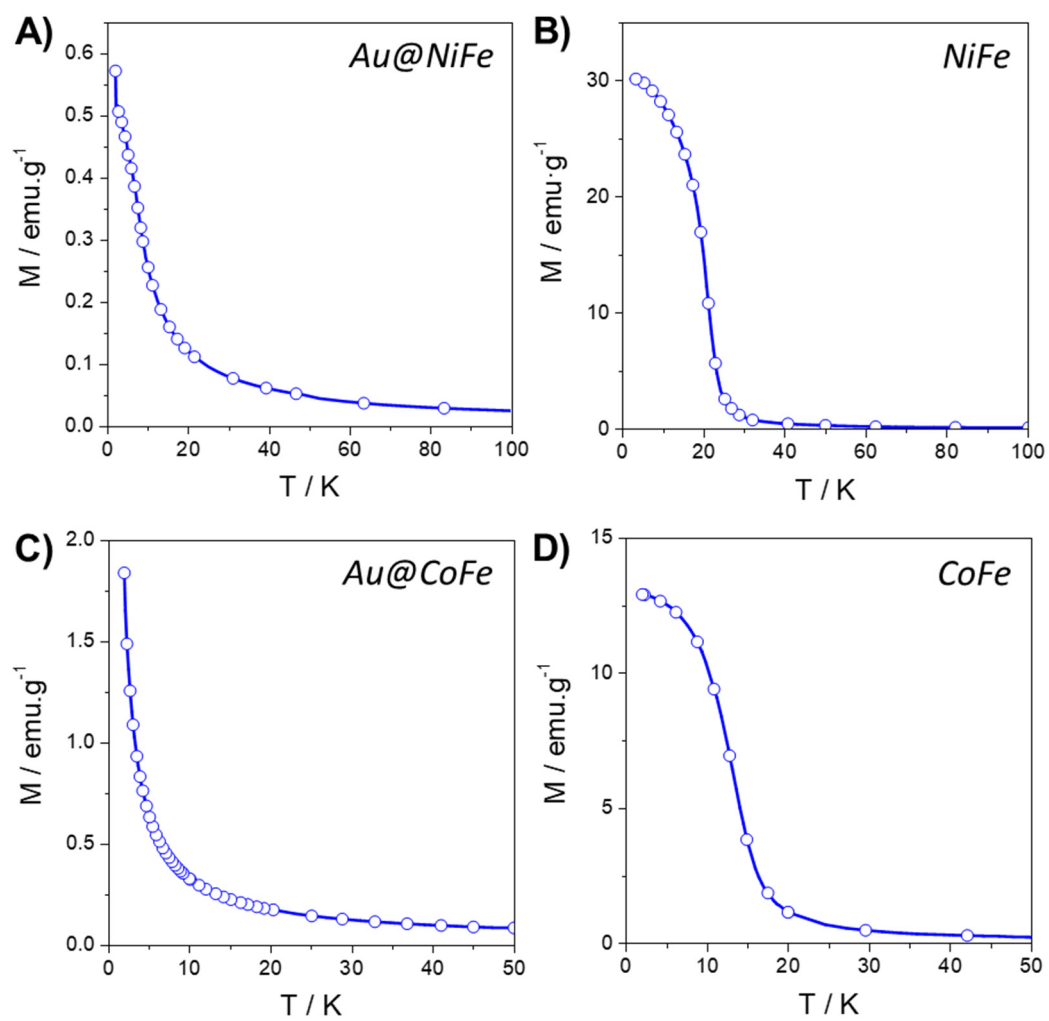**Figure S2.** A) B) UV-Vis spectra of Au and the different Au@PBA NPs. C) D) Plasmon position and plasmon FWHM calculated for the different NPs.
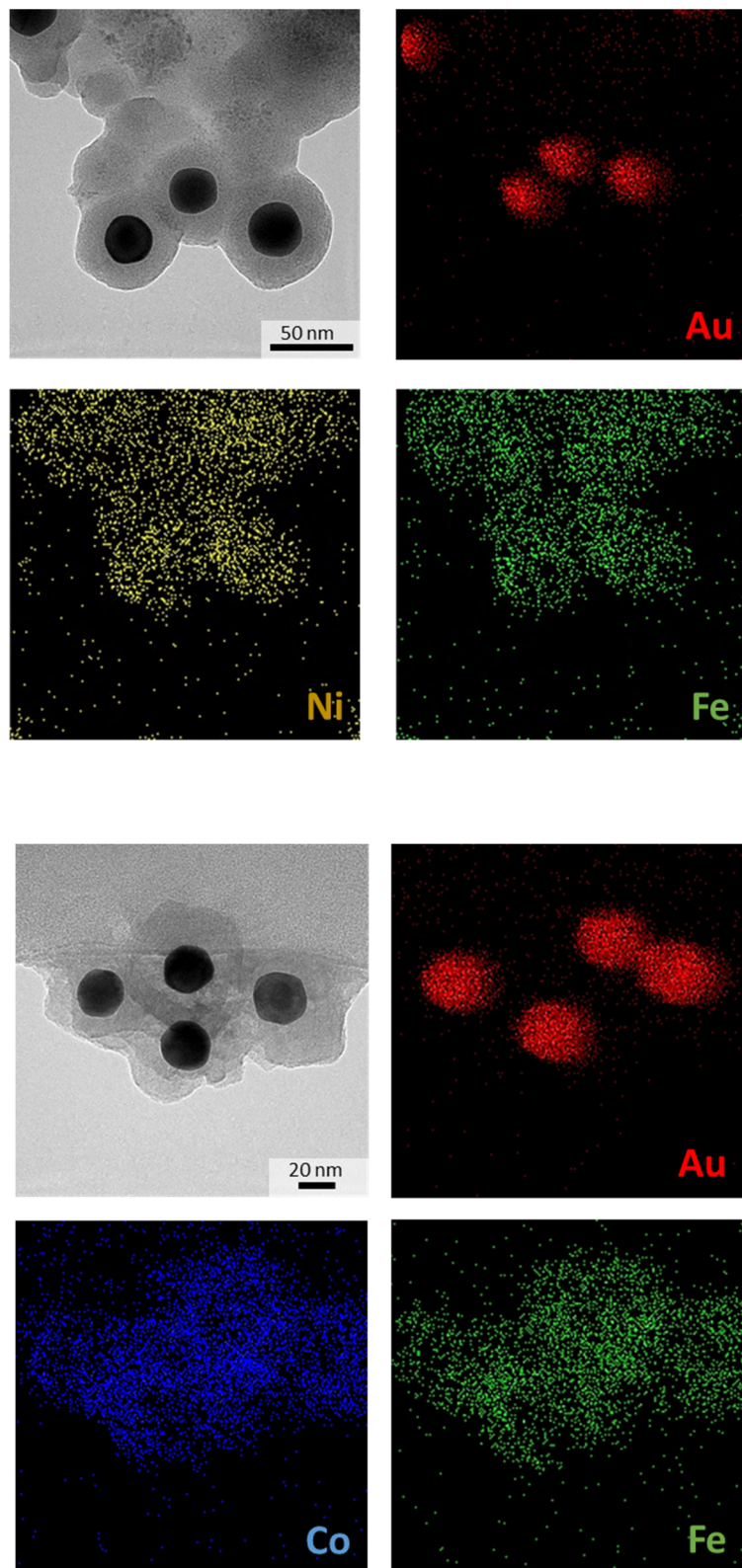
Figure S3. EDX mapping of the metals present in the Au@PBA(thin) heterostructures.
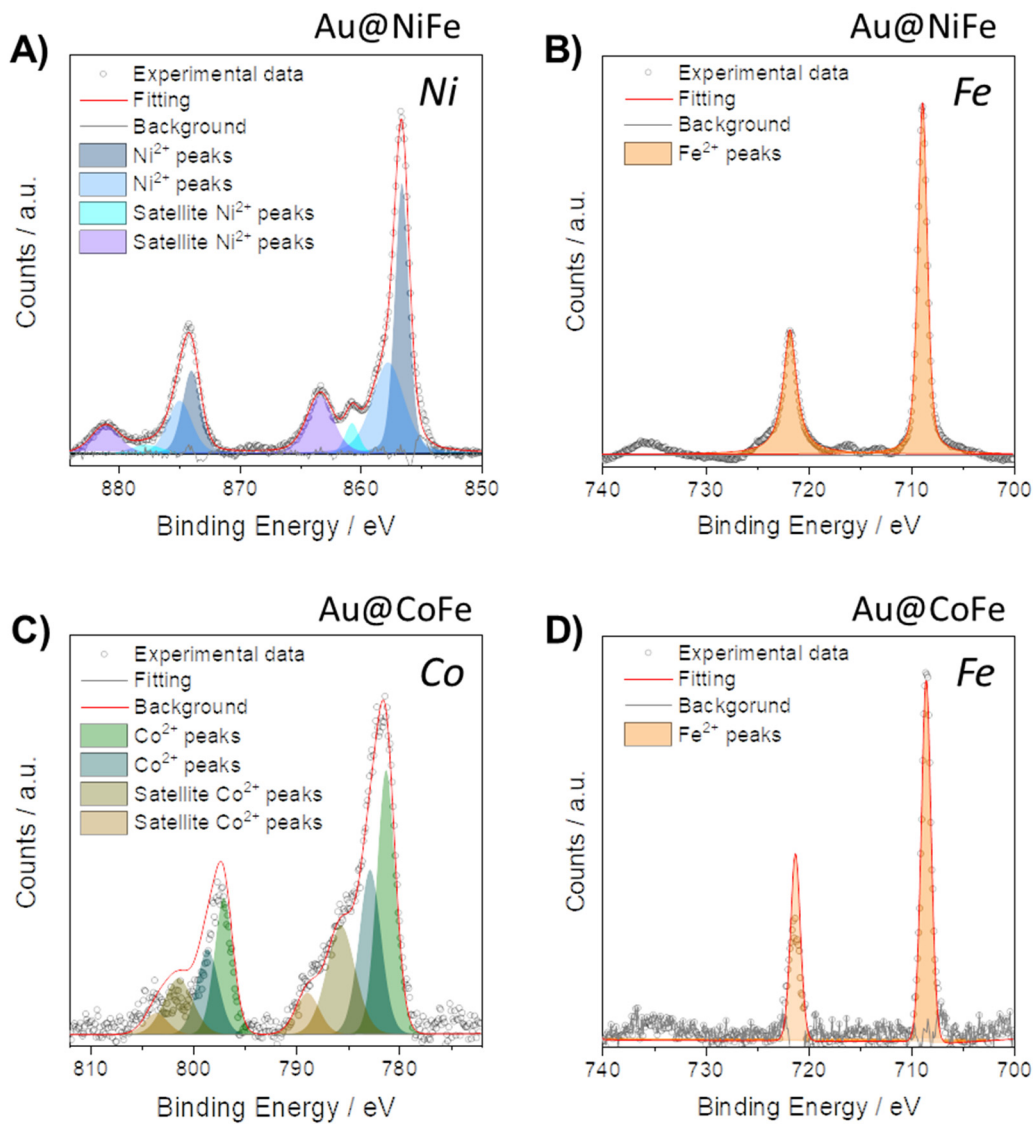
Figure S4. XPS spectra of Au@NiFe (up) and Au@CoFe (down).

Figure S5. Magnetization vs. temperature curve performed for Au@NiFe and NIFe-PBA (up) and Au@CoFe and CoFe-PBA (down) nanoparticles with an applied field of 1000 Oe.
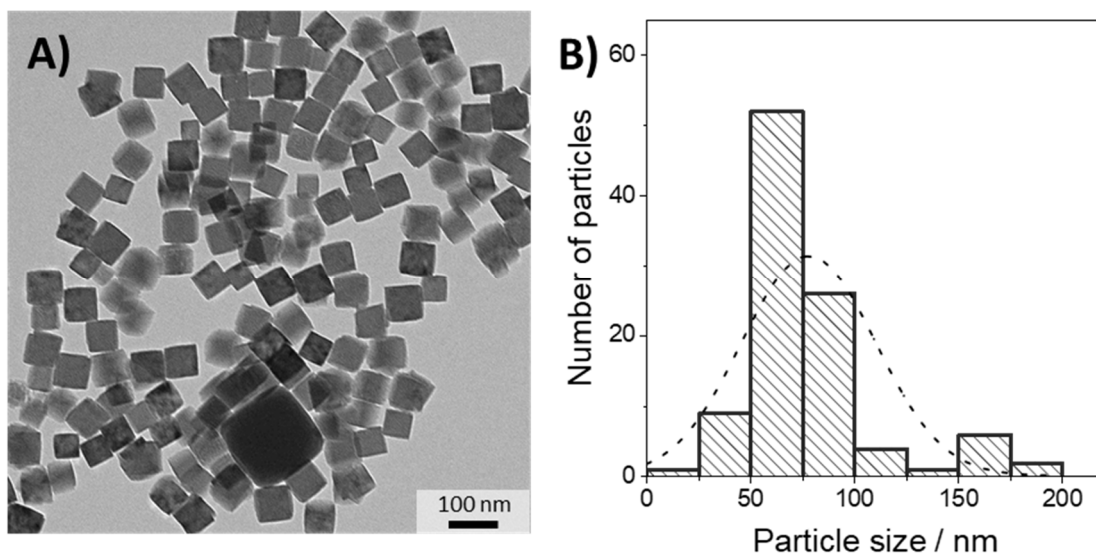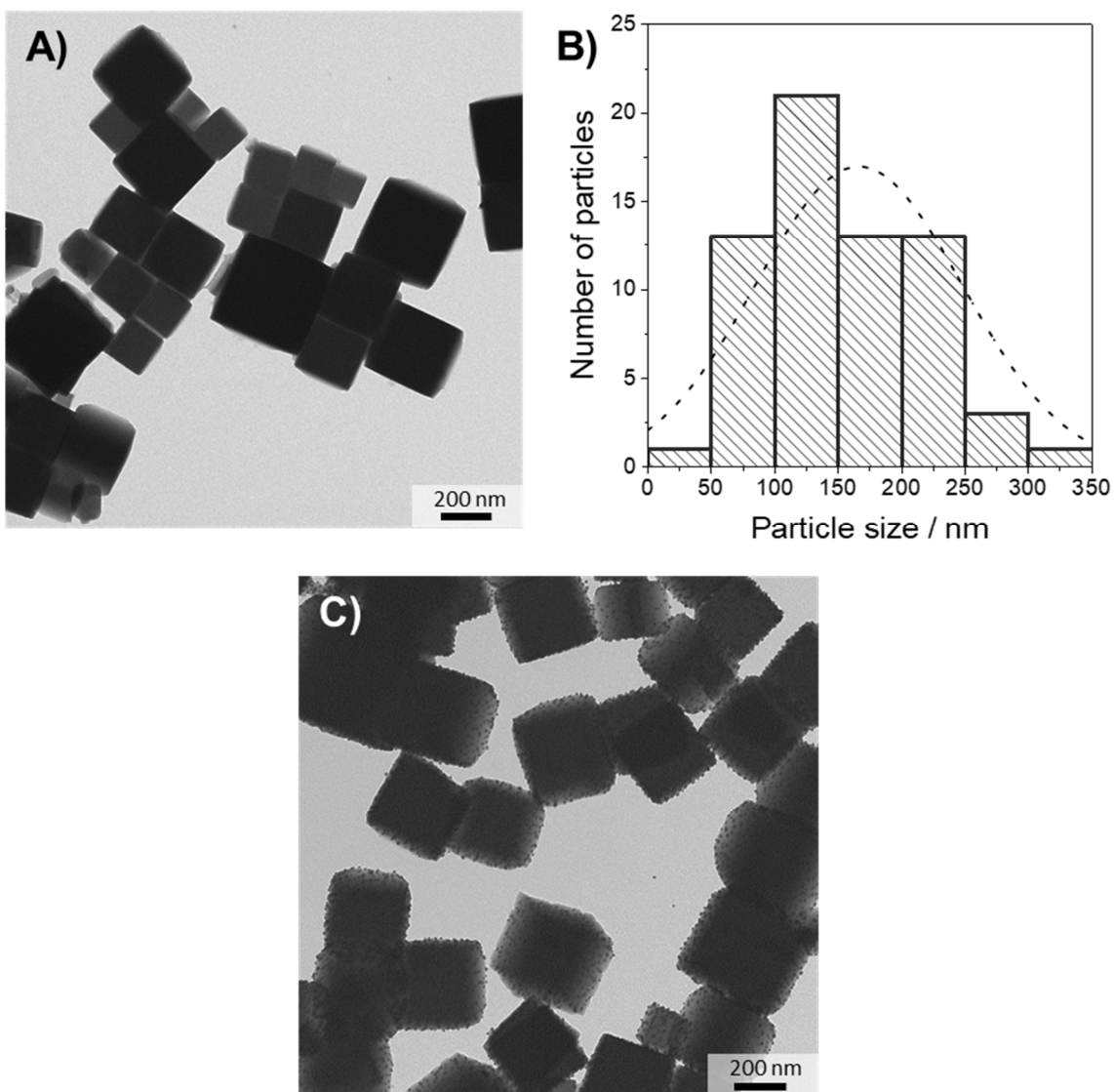
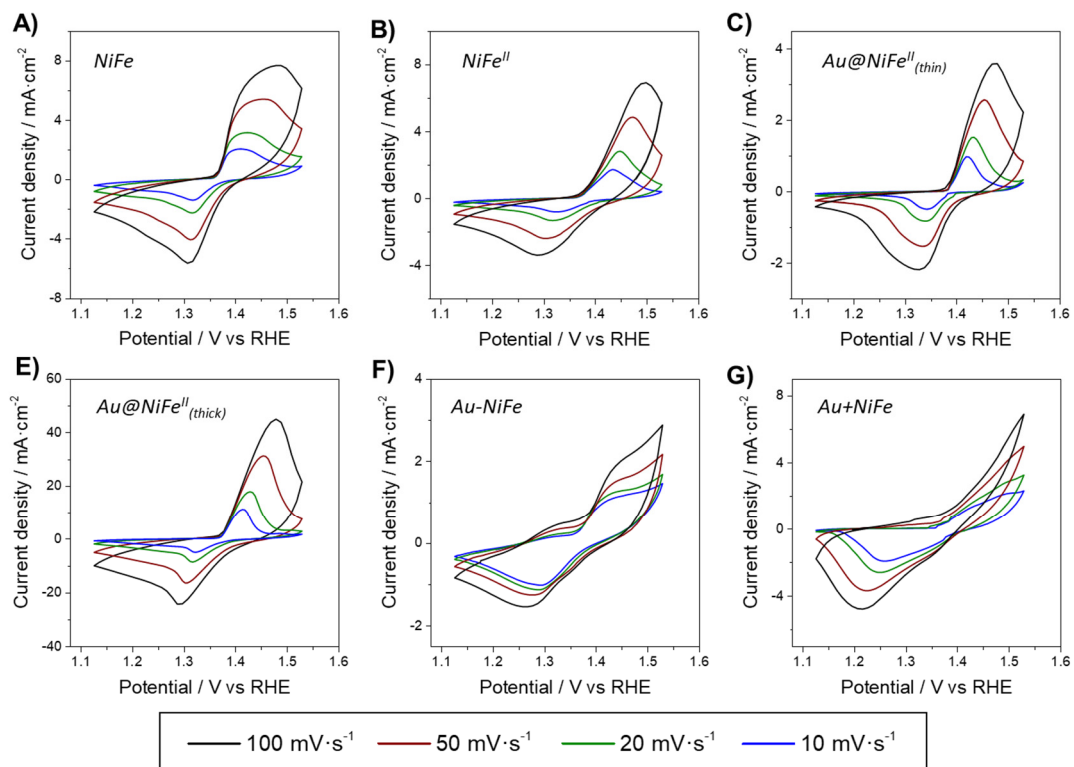**Figure S6.** PBA-NiFe^{II} NPs and its corresponding histogram.
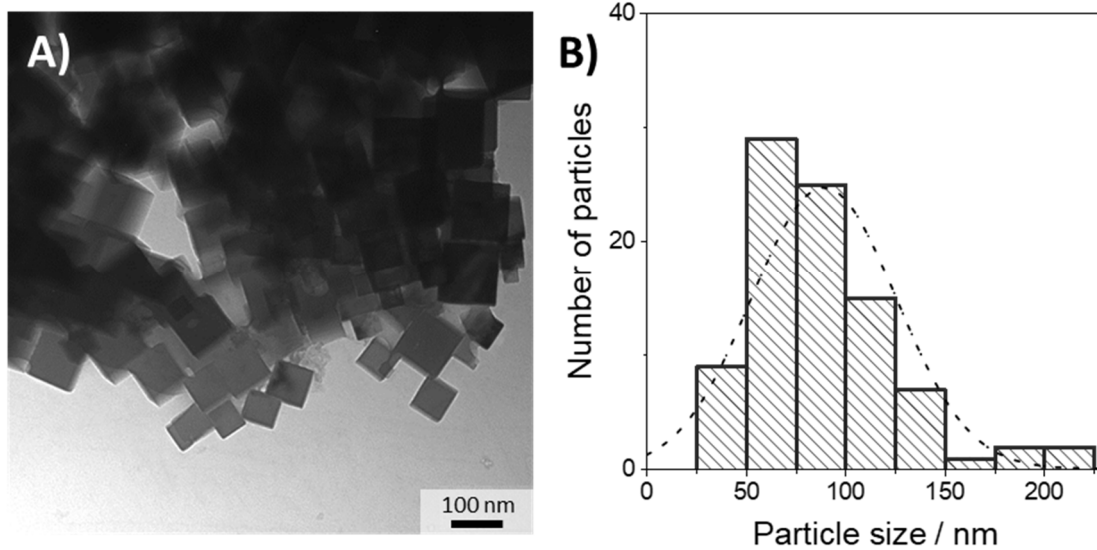
**Figure S7.** PBA-CoFe^{II} NPs and its corresponding histogram.
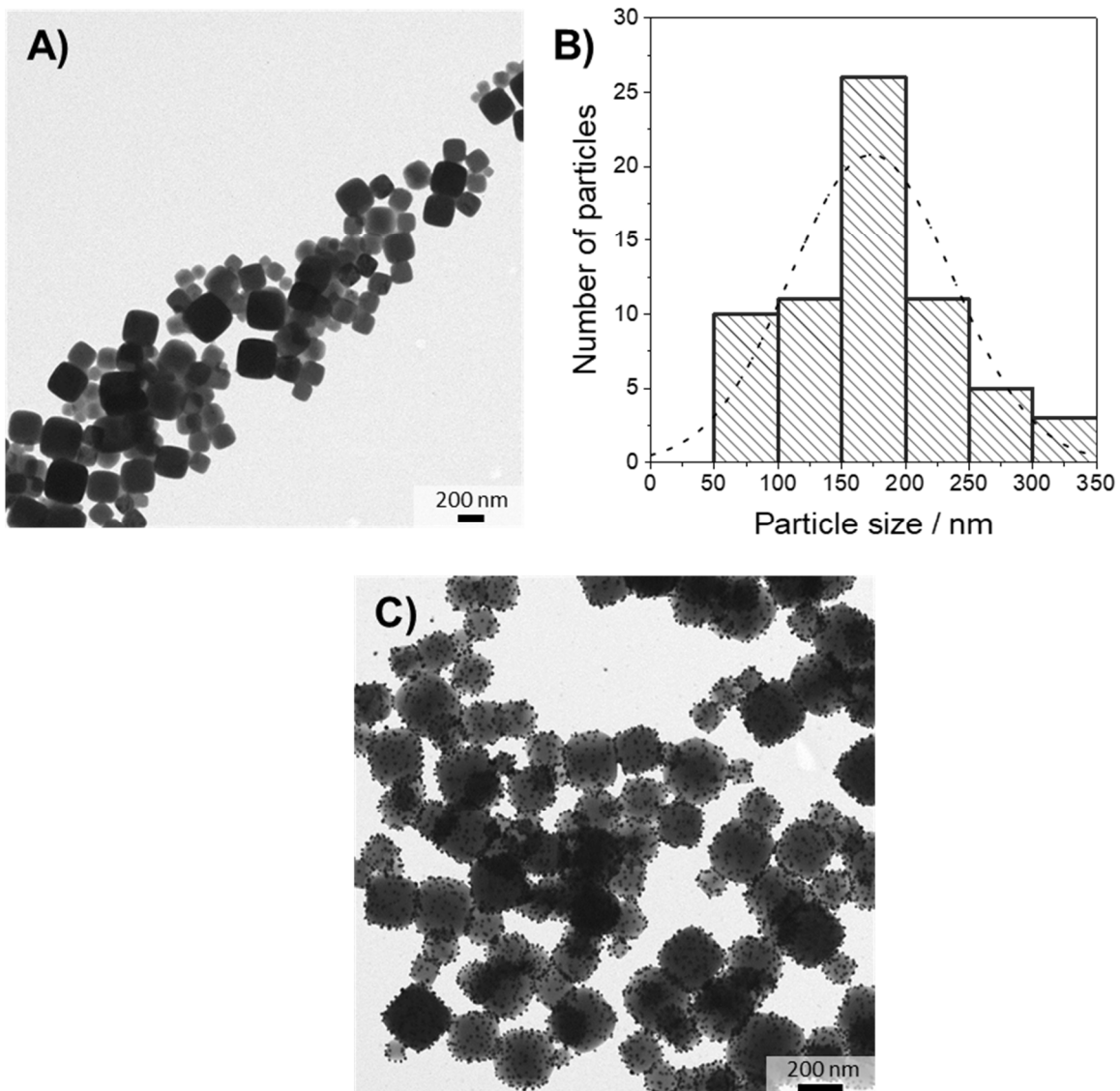
**Figure S8.** A) B) PBA-NiFe NPs and its corresponding histogram. C) Au-decorated PBA-NiFe NPs.

Figure S9. A) B) PBA-CoFe NPs and its corresponding histogram. C) Au-decorated PBA-CoFe NPs.
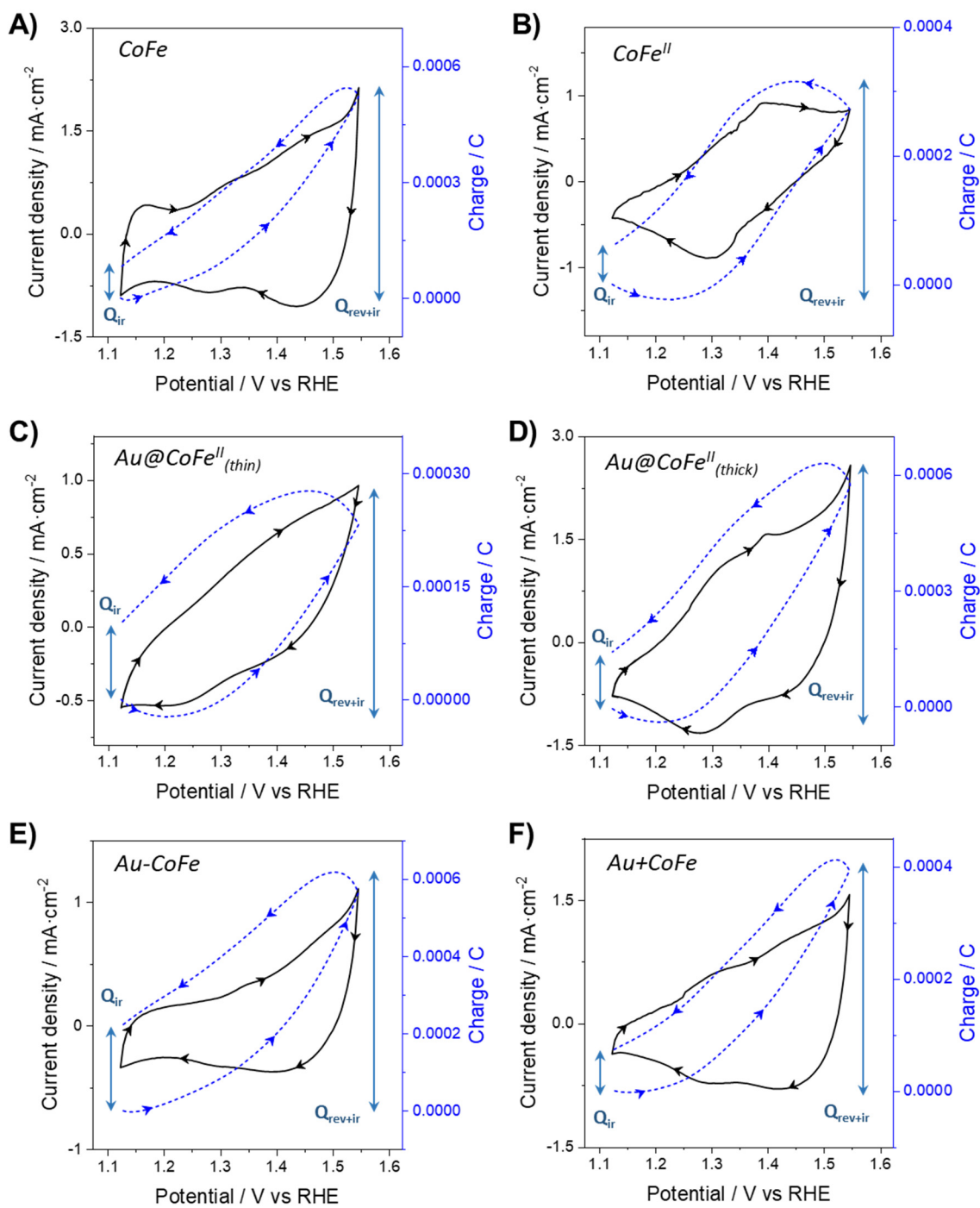
Figure S10. Voltammetric responses to potential cycles performed at different scan rates in 1 M KOH aqueous solution for different NiFe nanoparticles: A) PBA, B) PBA with Fe^{II}, C) Au@PBA (thin shell), D) Au@PBA (thick shell), E) Au decorated PBA NPs and F) physical mixture of Au and PBA NPs.
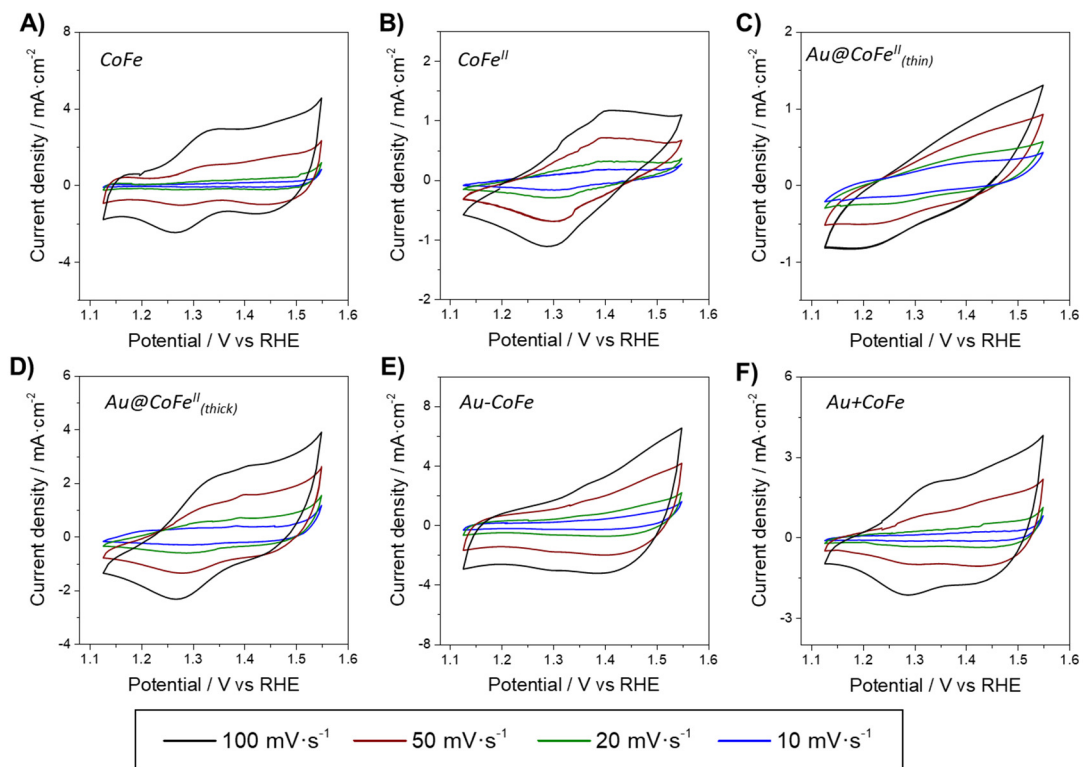
Figure S11. Voltammetric responses to potential cycles performed at different scan rates in 1 M KOH aqueous solution for different CoFe nanoparticles: A) PBA, B) PBA with Fe^{II}, C) Au@PBA (thin shell), D) Au@PBA (thick shell), E) Au decorated PBA NPs and F) physical mixture of Au and PBA NPs.
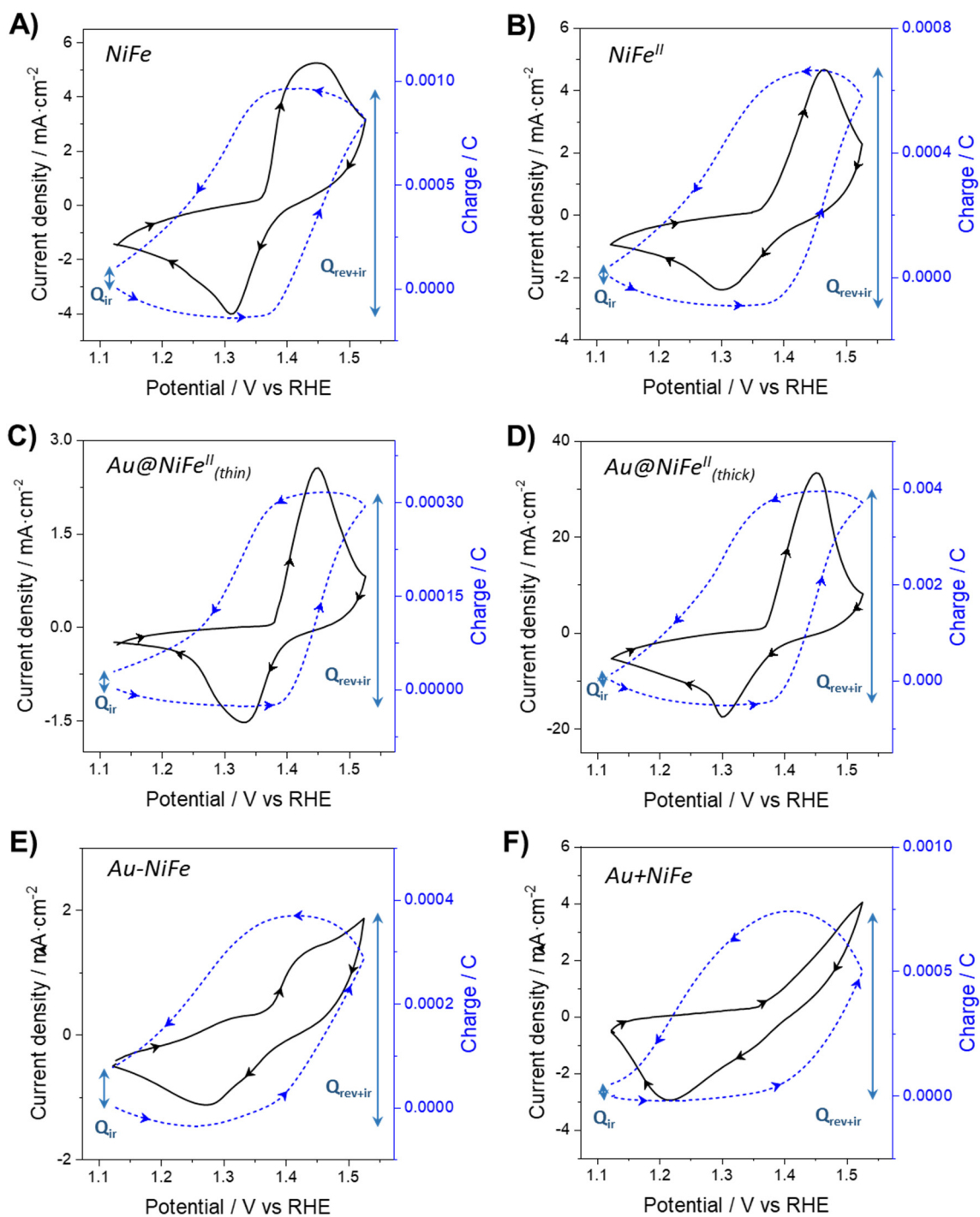
Figure S12. Evolution of the consumed charge (coulovoltammetric response) parallel to the voltammetric response to the cyclic voltammetry performed at 50 mV·s^{-1} in 1 M KOH aqueous solution for NiFe compounds.

Figure S13. Evolution of the consumed charge during the voltammetric responses parallel to potential cycles performed at 50 mV·s^{-1} in 1 M KOH aqueous solution for CoFe compounds.

Table S1. Amount of electroactive PBA mass being reversibly oxidized/reduced during cyclovoltamperometric experiments.

Samples	PBA mass (mg/cm^2)	z = 1		z = 2	
		PBA e.a. mass (mg/cm^2)	PBA e.a. (%)	PBA e.a. mass (mg/cm^2)	PBA e.a. (%)
NiFe	0.25	0.049	19.2	0.025	9.6
NiFe^{II}	0.25	0.031	10.9	0.015	5.5
Au@NiFe^{II}(thin)	0.14	0.017	13.6	0.008	6.8
Au@NiFe^{II}(thick)	0.23	0.174	72.0	0.087	36.0
Au@NiFe^{II}(very thick)	0.25	0.052	21.6	0.026	10.8
Au-NiFe	0.17	0.012	6.5	0.006	3.3
Au+NiFe	0.17	0.021	12.4	0.010	6.7
CoFe	0.25	0.016	6.3		
CoFe^{II}	0.25	0.012	4.5		
Au@CoFe^{II}(thin)	0.12	0.0074	5.4		
Au@CoFe^{II}(thick)	0.24	0.031	13.1		
Au-CoFe	0.18	0.013	6.9		
Au+CoFe	0.17	0.011	6.4		

The electroactive mass (e.a.) of PBA was estimated using Faraday's law of electrolysis:

$$m = \frac{Q}{F} \cdot \frac{M}{z}$$

Being, m the mass (g), Q the charge corresponding to the reversible redox process, M the molecular weight of the sample and z the total number of electrons taking part in the redox process.

Q was calculated by subtracting the total charge involving reversible and irreversible reactions (Q_{rev+ir}) and the charge consumed by the irreversible oxygen evolution, (Q_{ir}) calculated in Figures S12 and S13. The reversible charge allows the calculations of the number of electroactive metal atoms.

The redox processes of NiFe compounds are associated with the oxidation/reduction of Ni. Here, the initial Ni^{2+} is firstly oxidized to a mixed valance state of Ni^{3+}/Ni^{4+}. Therefore, calculations were carried out considering one (z = 1) or two (z = 2) electrons involved in the reaction.

For CoFe compounds, the redox processes associated with the reaction of Co^{2+} and Co^{3+} involves one electron (z = 1).
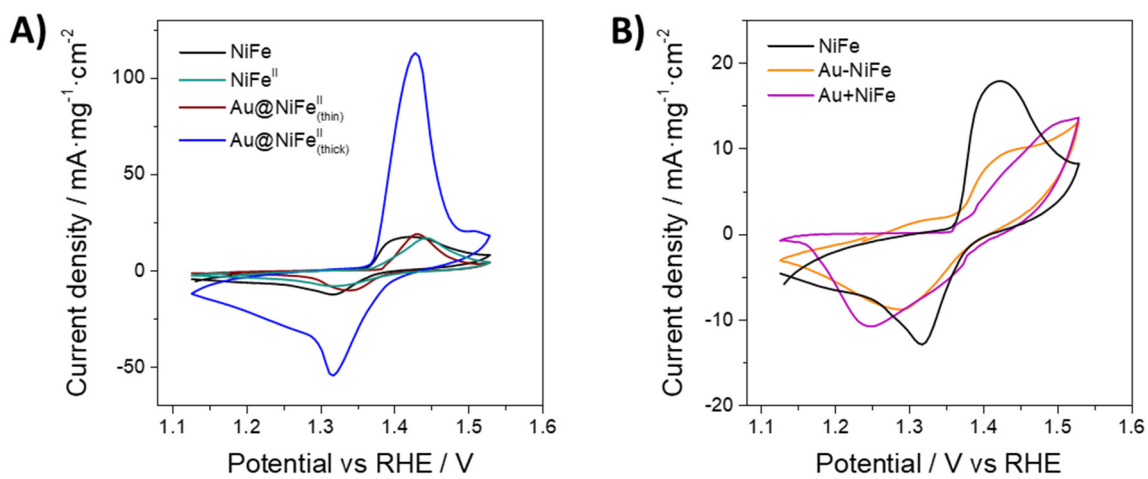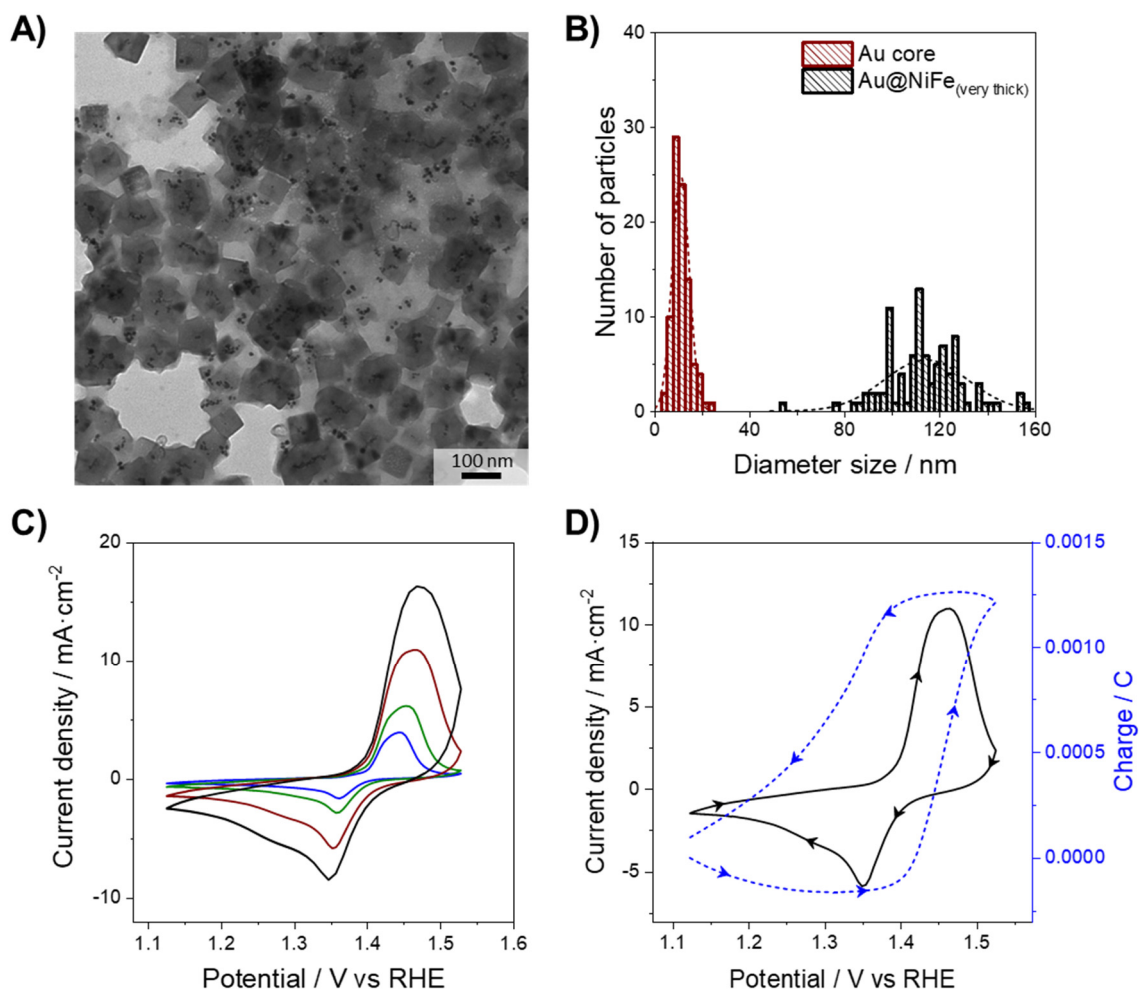
Figure S14. Voltammetric responses to potential cycles performed at 20 mV·s^{-1} in 1 M KOH aqueous solution for NiFe compound compared to: A) NiFe(II) and the electroactive species of Au@NiFe(thin) and Au@NiFe(thick); and B) the electroactive species of Au-NiFe and Au+NiFe.
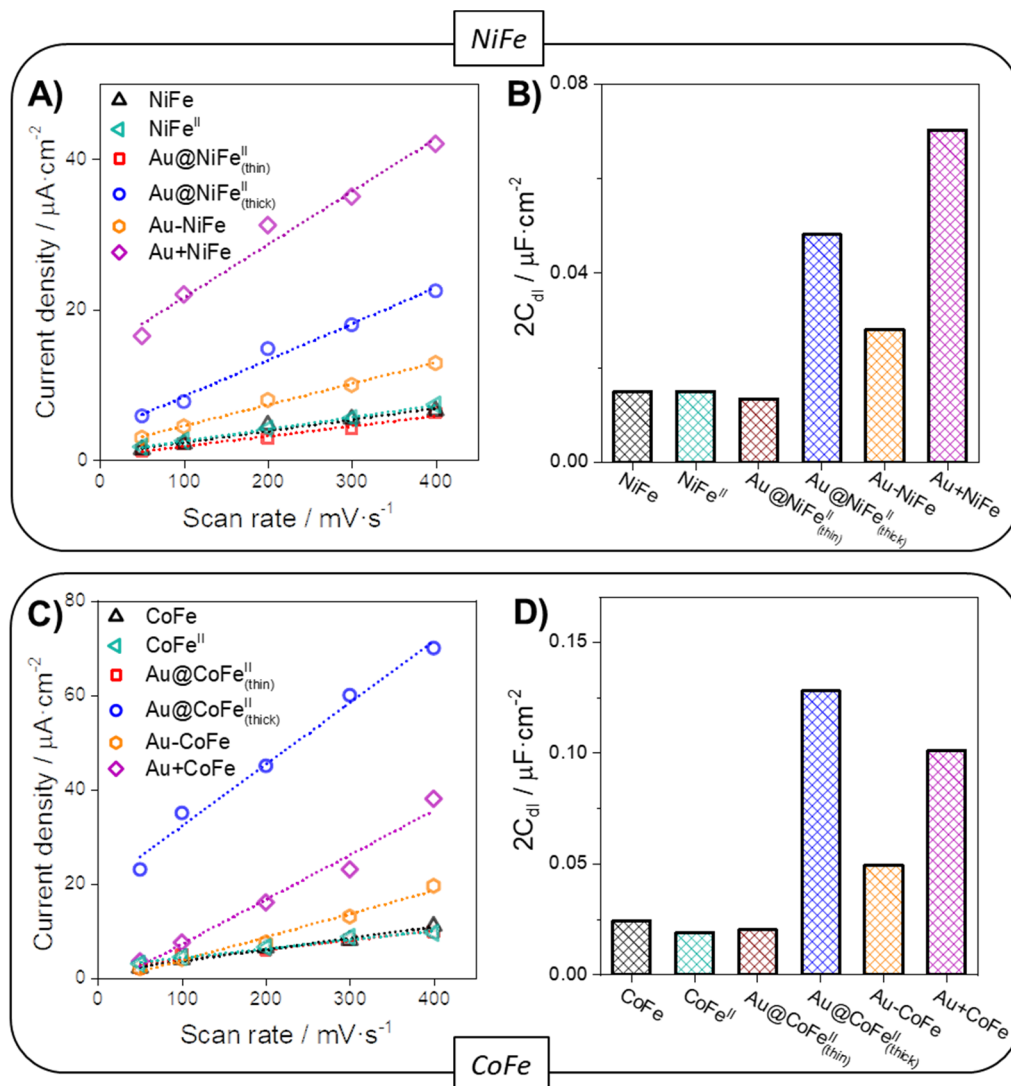
Figure S15. Linear slopes representing the ECSA calculated from CVs performed in a non-faradaic region at different scan rates for NiFe (A) and CoFe (C) PBA compounds. ECSA values of the different NPs of NiFe (B) and CoFe (D) PBA compounds.
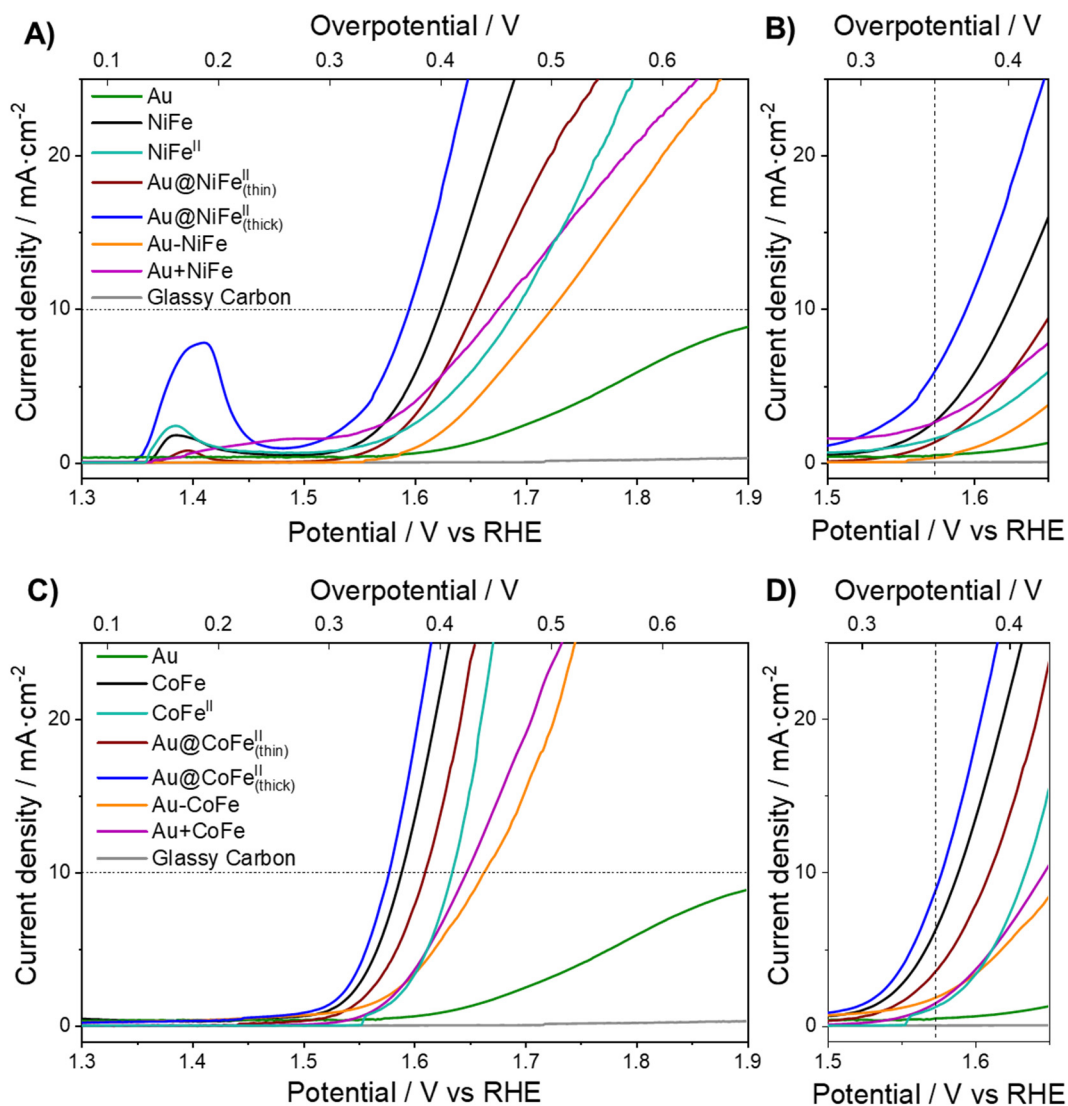
Figure S16. A) Linear Sweep Voltammetry of the different NiFe NPs. B) Zoom of Figure S16A exhibiting the beginning of the OER of the different NiFe NPs. C) Linear Sweep Voltammetry of the different CoFe NPs. D) Zoom of Figure S16CA exhibiting the beginning of the OER of the different CoFe NPs. All experiments were measured at 5 mV·s⁻¹ in 1 M KOH aqueous solution.

Figure S17. A) TEM image and B) histogram of the size distribution for Au@NiFe NPs with a very thick shell. C) Voltammetric responses to potential cycles performed at 100, 50, 20 and 5 mV·s^{-1} in 1 M KOH aqueous solution. D) Evolution of the consumed charge (coulovoltammetric response) parallel to the voltammetric response to the cyclic voltammetry performed at 50 mV·s^{-1} for Au@NiFe with a very thick shell.
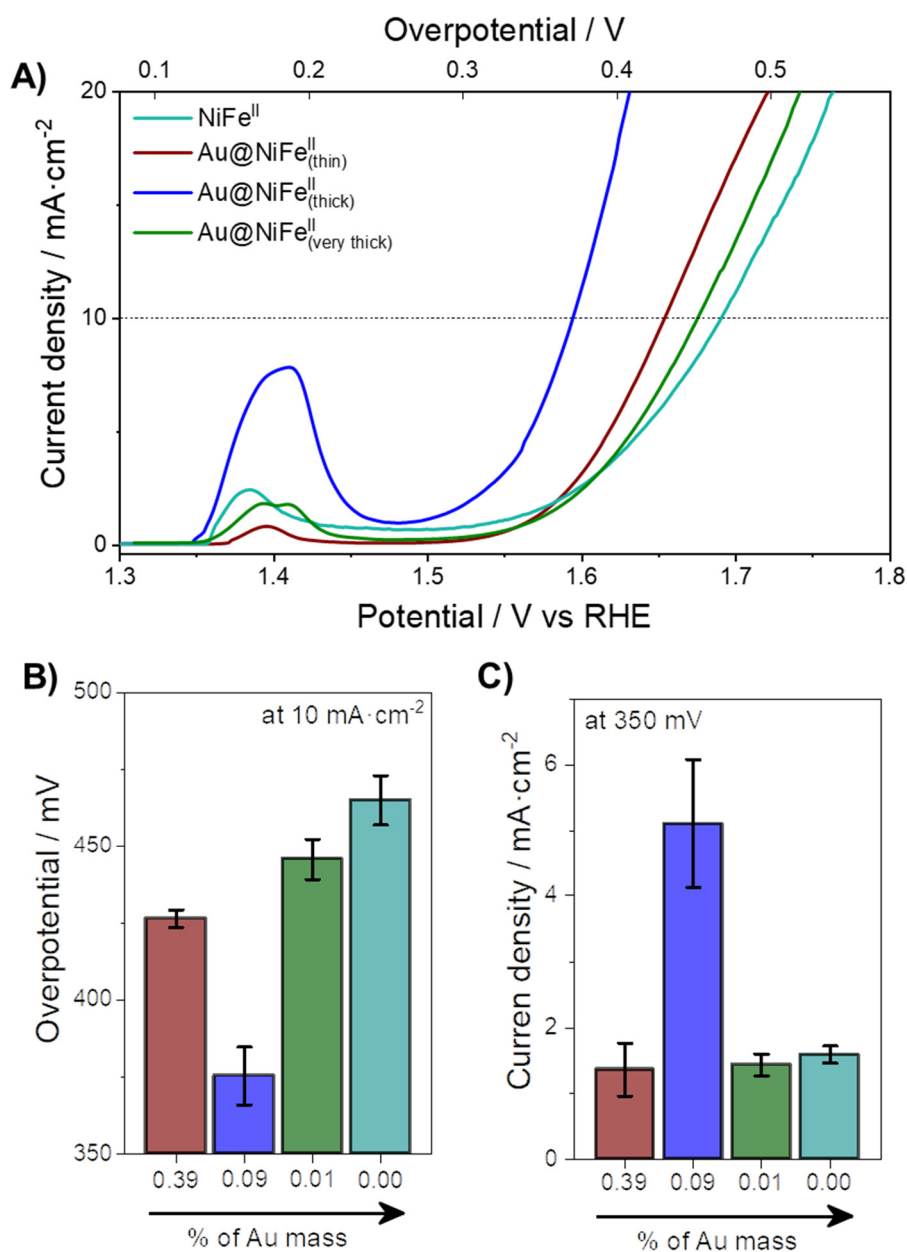
Figure S18. A) Linear Sweep Voltammetry of different Au@NiFe NPs measured at 5 mV·s⁻¹ in 1 M KOH aqueous solution. B) Overpotential required for a current density of 10 mA·cm⁻². D) Current density obtained at an overpotential of 350 mV.
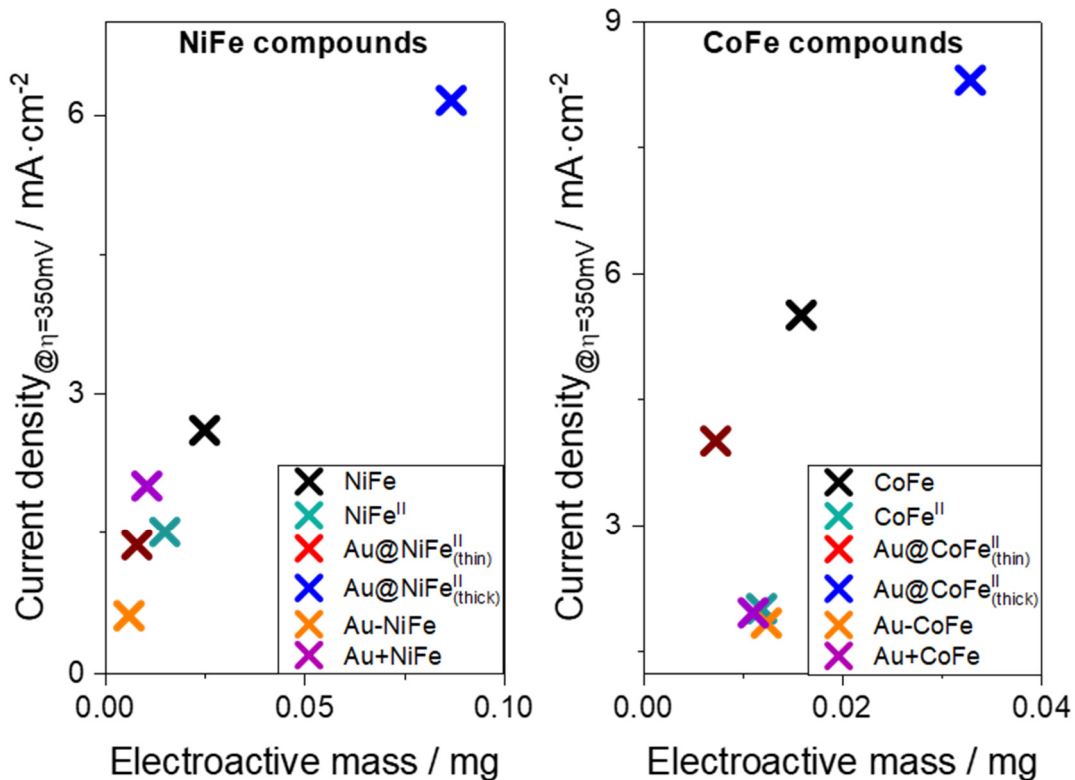
Figure S19. Current density at an overpotential of 350 mV plotted against the electroactive mass of the different PBA based nanoparticles.
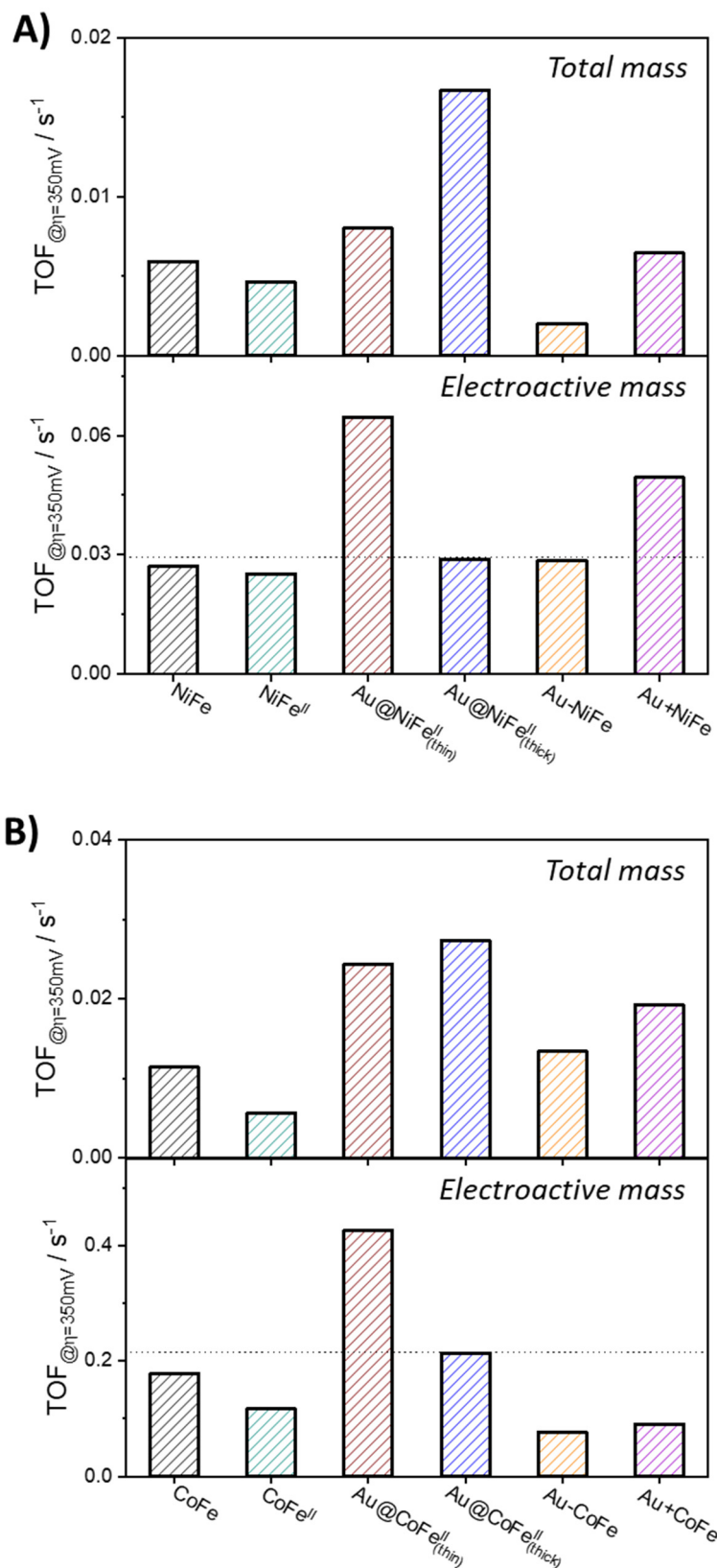
Figure S20. Turnover frequencies calculated at 0.35 V overpotential for NiFe compounds (A) and CoFe compounds (B). TOF values were calculated using the total PBA mass or the electroactive PBA mass previously obtained considering z = 1 (see Table S1).
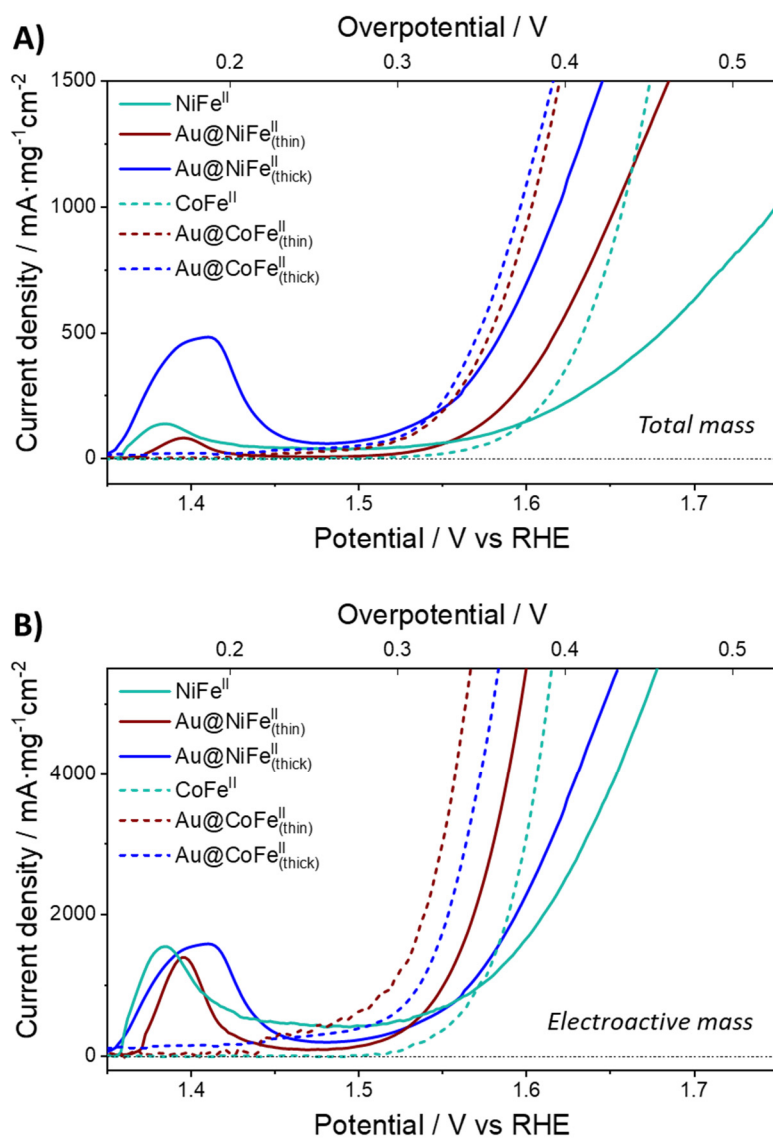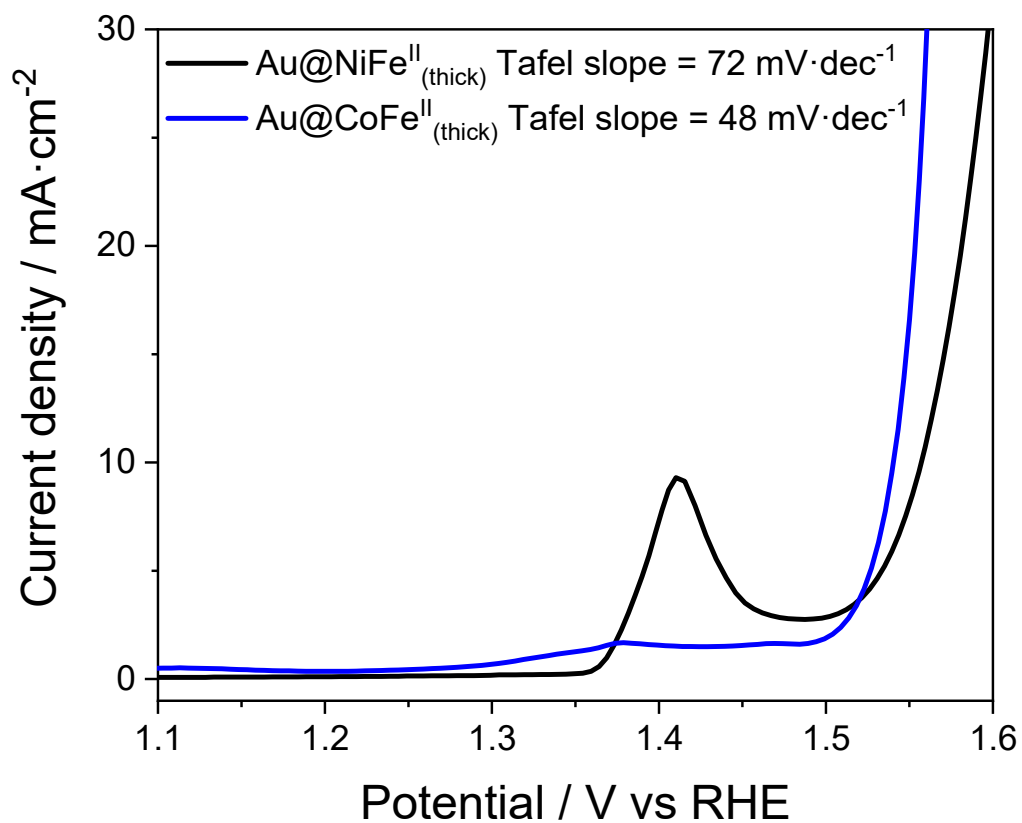
Figure S21. A) Linear Sweep Voltammetry of PBA (of Fe(II)), Au@PBA(thin) and Au@PBA(thick) NPs measured at 5 mV·s⁻¹ in 1 M KOH aqueous solution. The current densities were normalized considering A) the total PBA mass and B) the electroactive PBA mass.
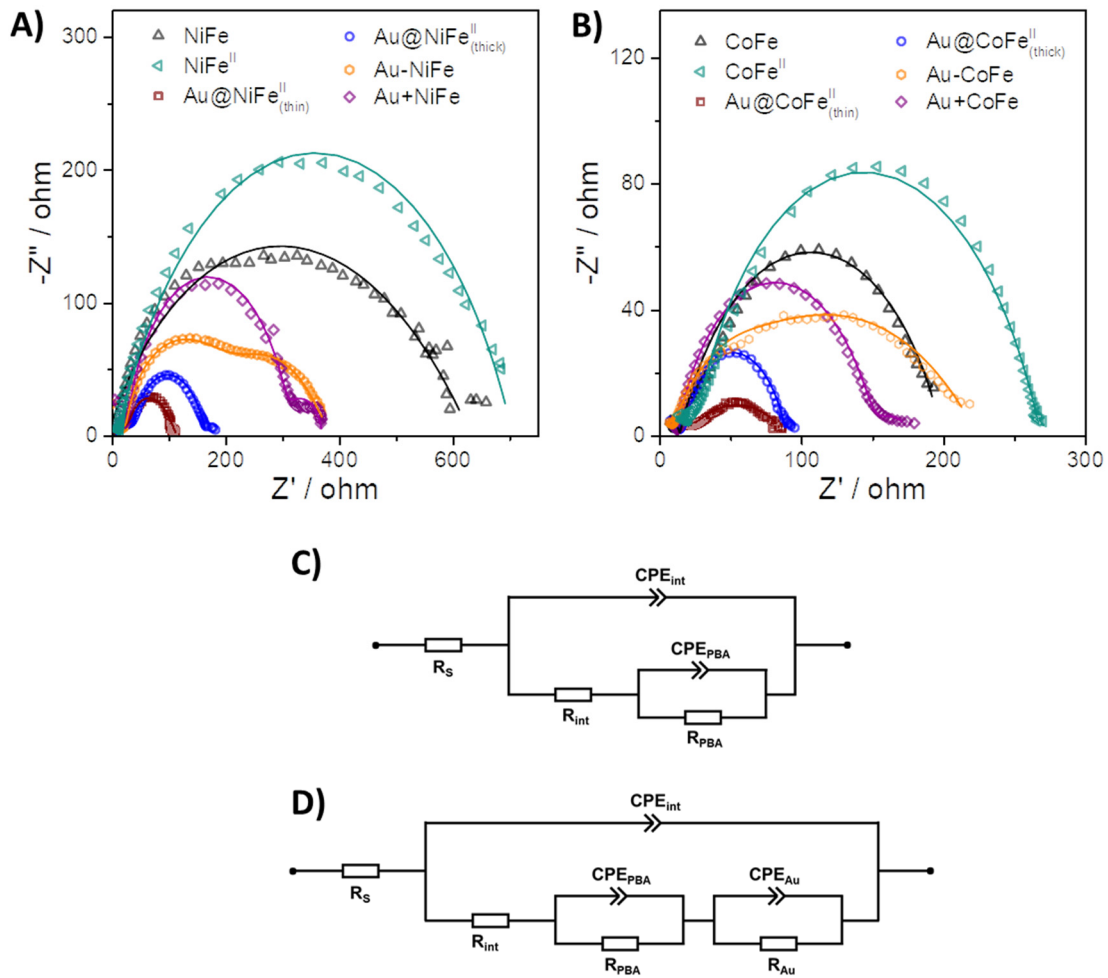
Figure S22. A) B) Nyquist plots of the different samples recorded at an overpotential of 0.4 V. Points correspond to experimental data, and lines are curves fitted with the equivalent circuit. C) Equivalent circuit used for the two PBA NPs, Au@PBA(thin) and Au@PBA(thick). D) Equivalent circuit used for Au-PBA and Au+PBA.

**Table S2.** Comparison of the electrocatalytic activity with previous reported OER electrocatalysts.

| Sample	Potential at 10 mA·cm^{-2} (V vs RHE)	Solution	*iR* correction	Electrode	Reference
Au@NiFe	1.59	1M KOH	no	GC	This work
Au@CoFe	1.57	1M KOH	no	GC	This work
Au@NiFe	1.55	1M KOH	yes	Ni foam	This work
Au@CoFe	1.53	1M KOH	yes	Ni foam	This work
Au@Co$_3$O$_4$	1.61	0.1 M KOH	yes	GC	3
Au@CoFeO$_x$	1.55	1M KOH	yes	GC	4
Au@NiO	1.63	1M KOH	yes	GC	4
CoFe LDH	1.65	1M KOH	no	GC	5
NiFe LDH	1.58	1M KOH	yes	GC	6
IrO$_2$	1.57	1M KOH	yes	GC	6
CNTs-Au@Co$_3$O$_4$	1.58	1M KOH	no	GC	7
NiFe-v$_{CN-}$ PBA	1.513	1M KOH	yes	RDE GC	8
CoFe-v$_{CN-}$ PBA	1.599	1M KOH	yes	RDE GC	8
ZnCo$_2$O$_4$/A u/CNTs	1.67	1M KOH	no	RDE GC	9
NiO-NiFe$_2$O$_4$/rGO	1.53	1M KOH	no	RDE GC	10
CoFe oxide	1.54	1M KOH	yes	Ni foam	11
CoFe film PBA	1.66	0.1M KOH	no	FTO glass	12
Au/NiFe LDH	1.467	1M KOH	yes	Ti mesh	13
Ag@Co(OH)$_2$	1.48	1M KOH	no	Carbon cloth	14
Ag+Co(OH)$_2$	1.55	1M KOH	no	Carbon cloth	14

Figure S23. Linear Sweep Voltammetries performed in Ni foam substrate and with *iR* correction at 5 mV·s⁻¹ in 1 M KOH solution.
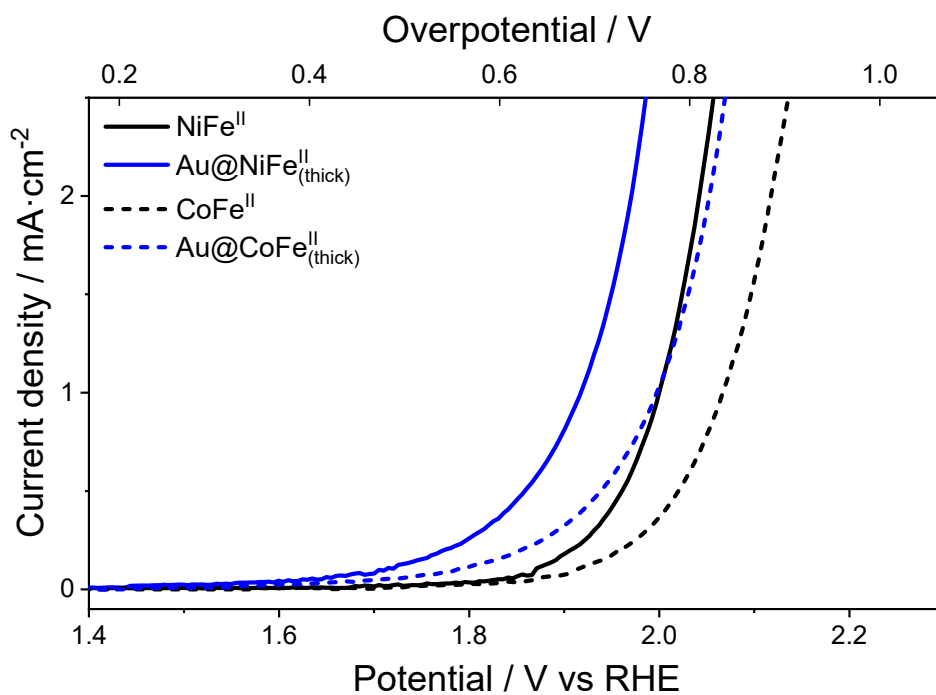
Figure S24. Linear Sweep Voltammetry of PBA (of Fe(II)) and Au@PBA(thick) NPs measured at 5 mV·s^{-1} in 0.5 M H$_2$SO$_4$ aqueous solution.
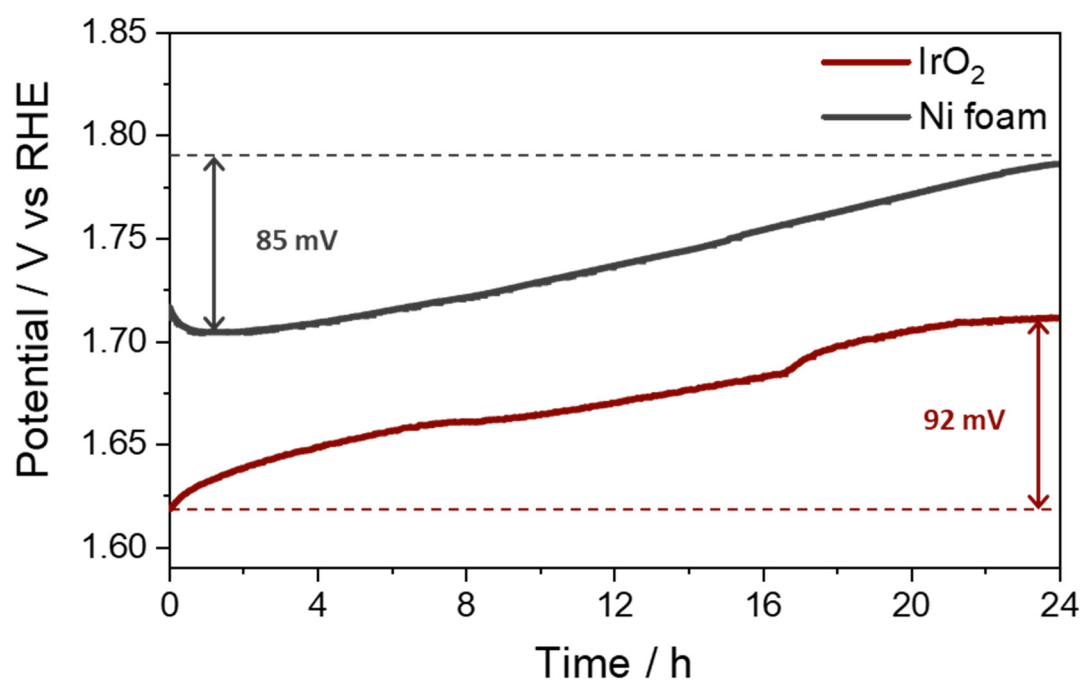
Figure S25. Stability of IrO$_2$ and the Ni foam substrate under a constant current density of 20 mA·cm^{-2} for 24 h.

Pt wire before the Au@PBA(thin) stability test

Pt wire after the Au@PBA(thin) stability test
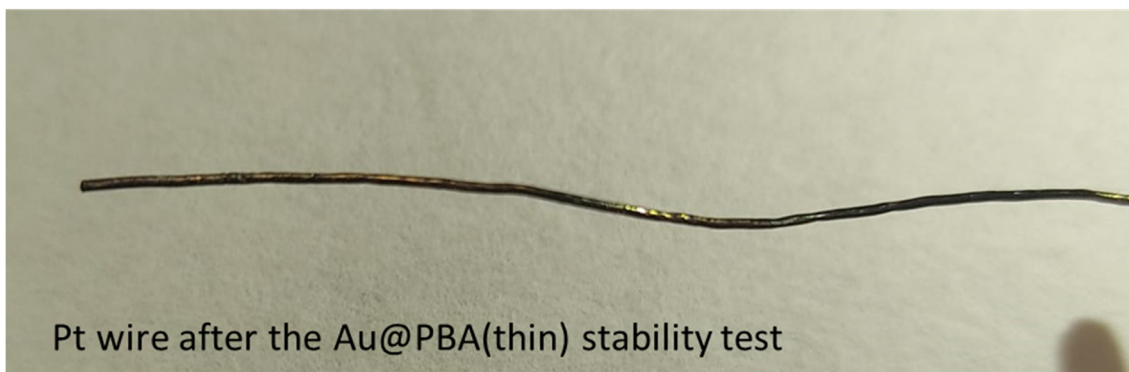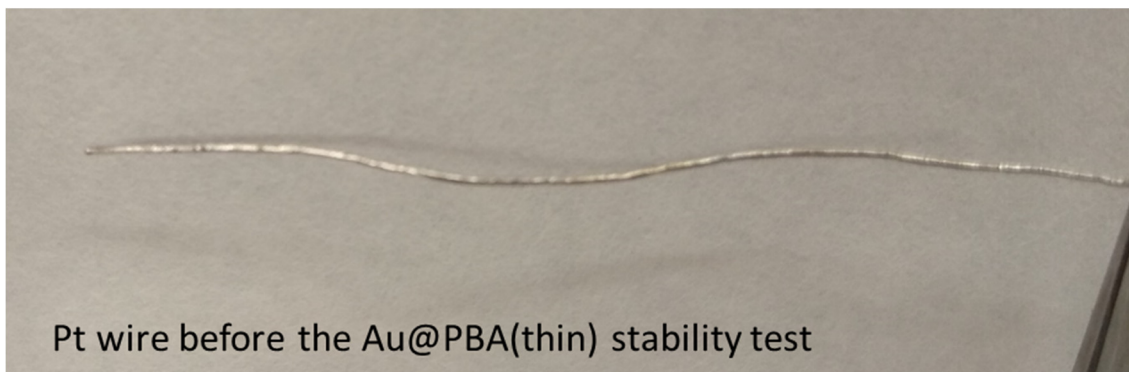
Figure S26. Photographies of the Pt wire (counter electrode) before and after the stability test of Au@PBA(thin) NPs. A yellowish color related to Au reduction can be observed after the measurement.
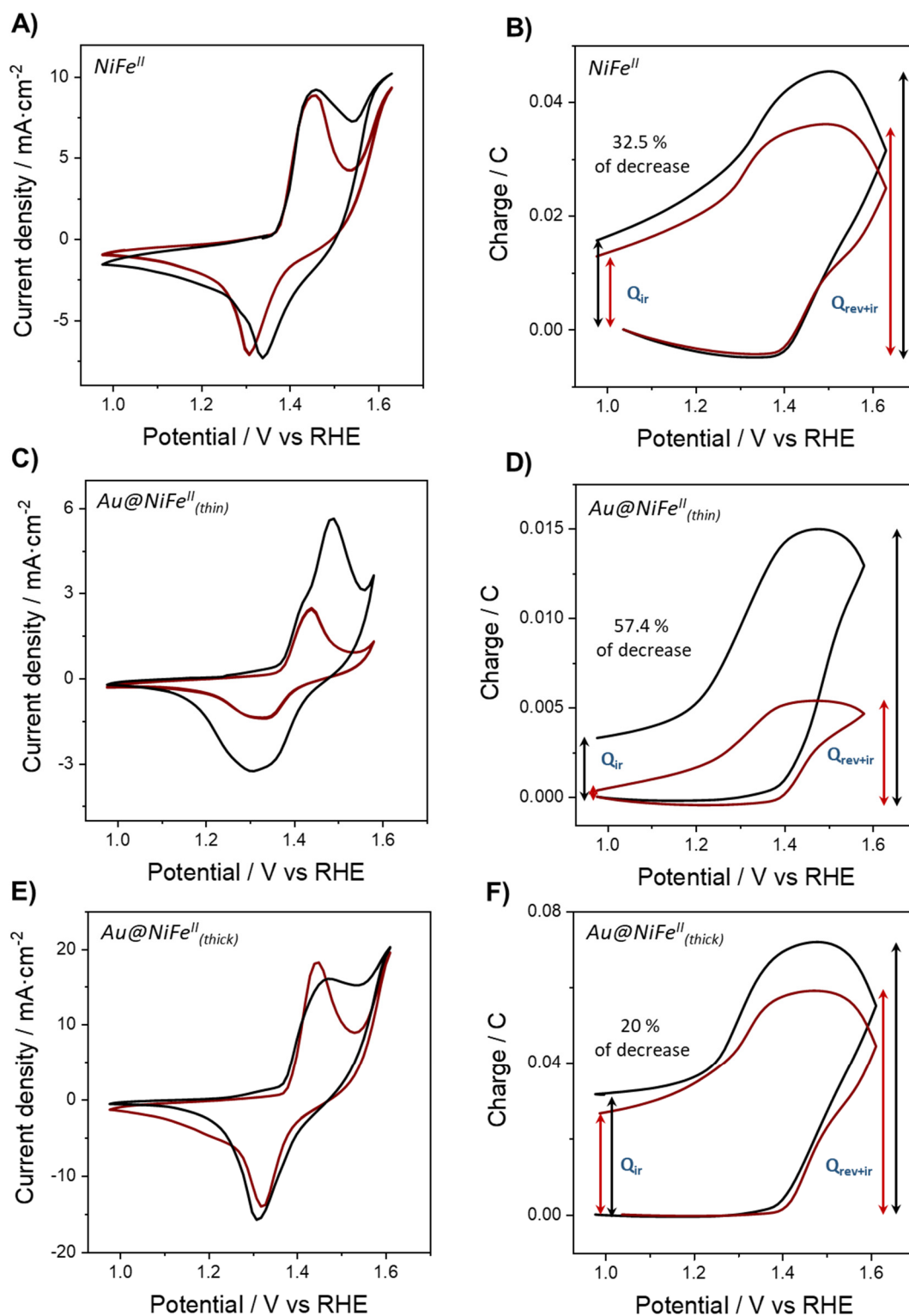
Figure S27. A) C) E) Voltammetric responses to potential cycles performed at 50 mV·s⁻¹ in 1 M KOH aqueous solution and B) D) F) evolution of the consumed charge (coulovoltammetric response) parallel to the voltammetric response to the cyclic voltammetry performed at 50 mV·s⁻¹ for NiFeᴵᴵ, Au@NiFe(thin) and Au@NiFe(thick) compounds before and after stability test. Black colors are referred to measurements before stability test and red colors are referred to measurements after stability test. The percentages correspond to the electroactive mass lost.
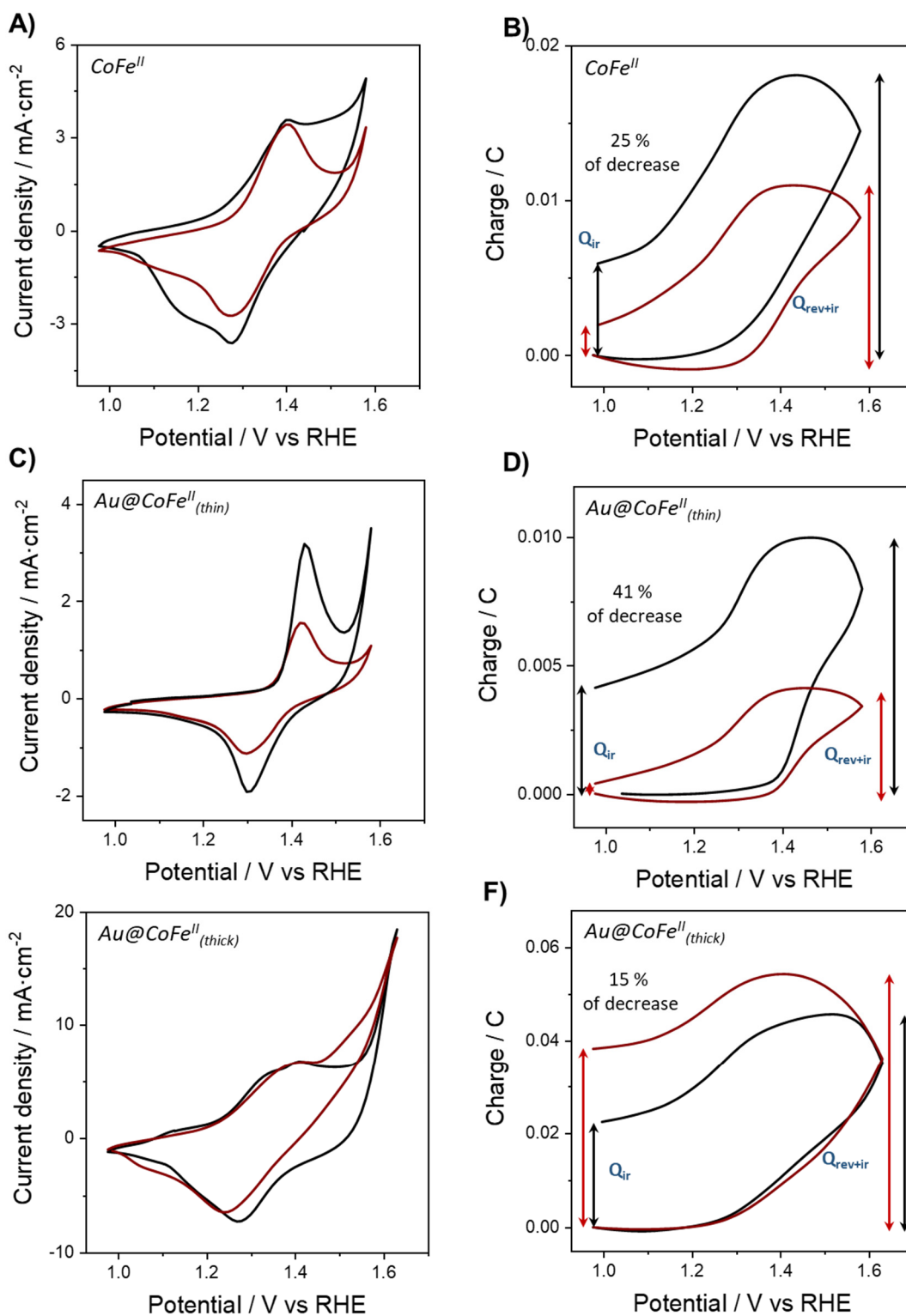
Figure S28. A) C) E) Voltammetric responses to potential cycles performed at 50 mV·s^{-1} in 1 M KOH aqueous solution and B) D) F) evolution of the consumed charge (coulovoltammetric response) parallel to the voltammetric response to the cyclic voltammetry performed at 50 mV·s^{-1} for CoFe^{II}, Au@CoFe(thin) and Au@CoFe(thick) compounds before and after stability test. Black colors are referred to measurements before stability test and red colors are referred to measurements after stability test. The percentages correspond to the electroactive mass lost.
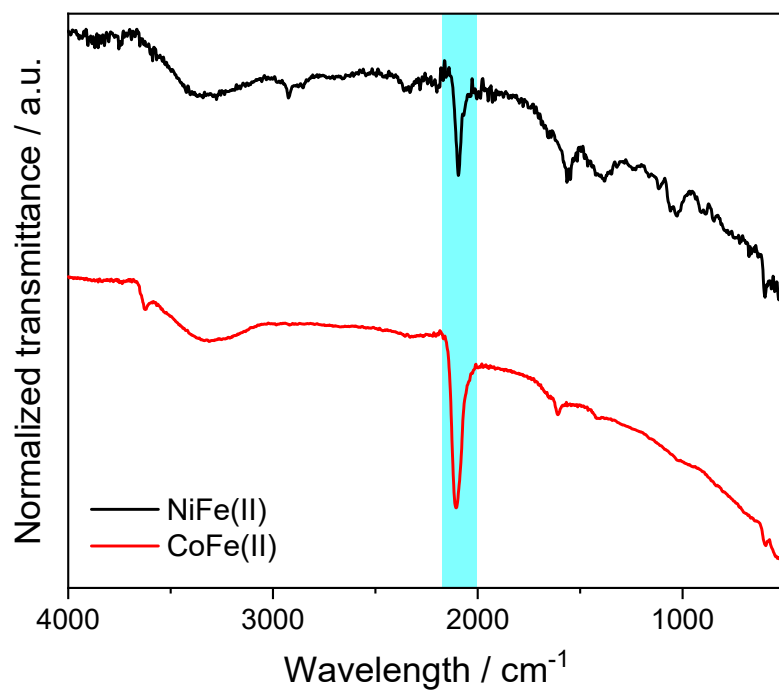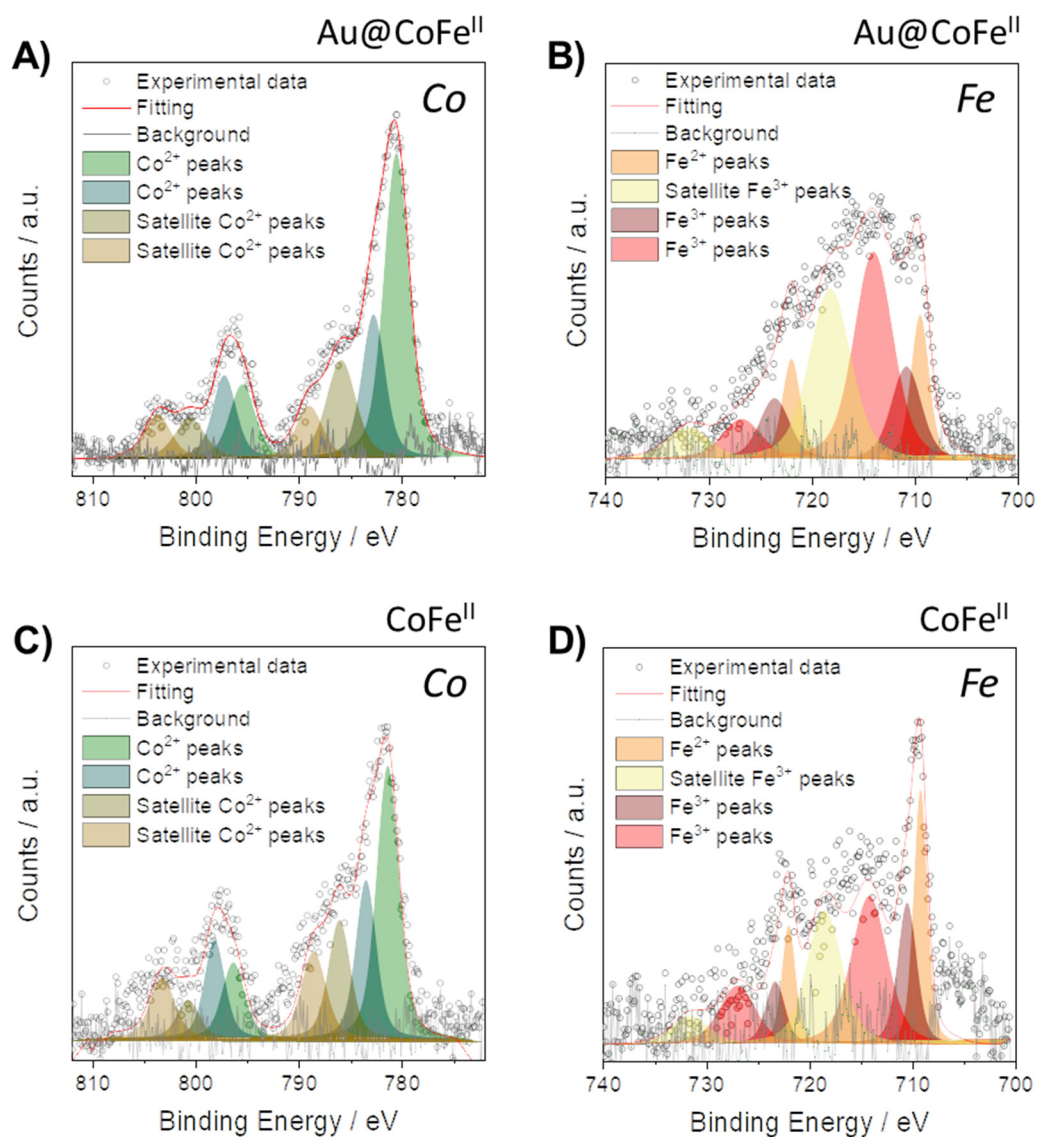
Figure S29. ATR-FTIR spectra of the NiFe(II) and the CoFe(II) NPs after the electrochemical stability test. The cyanide vibration peak is highlighted in blue.
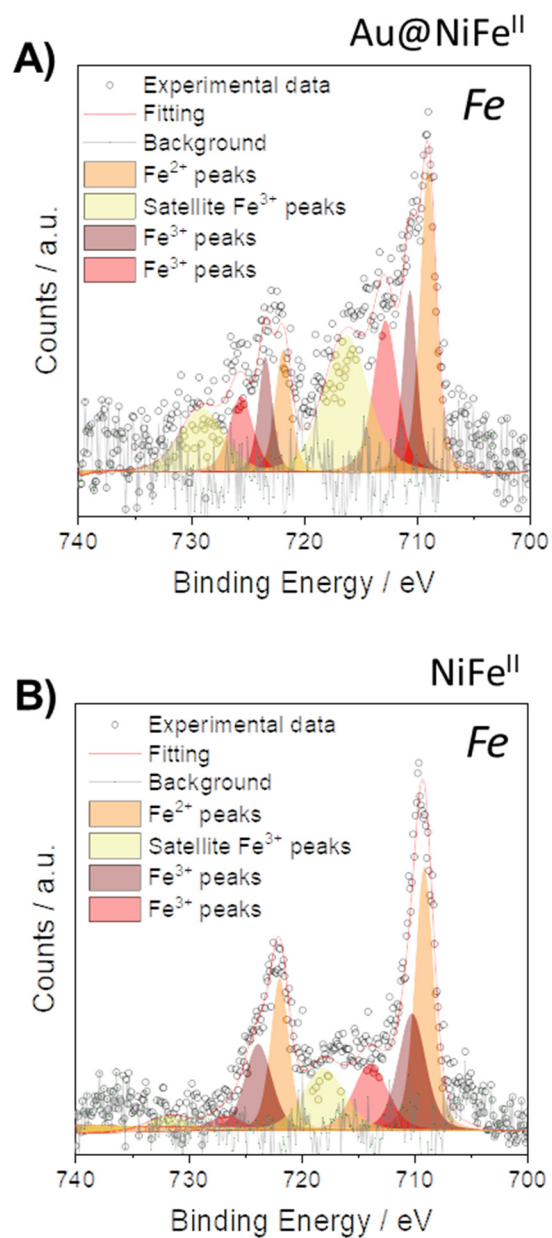
Figure S30. XPS spectra of Au@NiFe^{II} (up) and NiFe^{II} (down) after the electrochemical stability test. Ni spectra show mostly the contribution of Ni foam that masks the signal coming from the PBA.

Figure S31. XPS spectra of Au@CoFe^{II} (up) and CoFe^{II} (down) after the electrochemical stability test.

References

(1)   Turkevich, J. Colloidal Gold. Part I. Gold Bull. **1985**, 18 (4), 125–131.

(2)   Sanchis-Gual, R.; Susic, I.; Torres-Cavanillas, R.; Arenas-Esteban, D.; Bals, S.; Mallah, T.; Coronado-Puchau, M.; Coronado, E. The Design of Magneto-Plasmonic Nanostructures Formed by Magnetic Prussian Blue-Type Nanocrystals Decorated with Au Nanoparticles. Chem. Comm. **2021**, 57, 1903–1906.

(3)   Zhuang, Z.; Sheng, W.; Yan, Y. Synthesis of Monodispere $Au@Co_3O_4$ Core-Shell Nanocrystals and Their Enhanced Catalytic Activity for Oxygen Evolution Reaction. Adv. Mater. **2014**, 26 (23), 3950–3955.

(4)   Strickler, A. L.; Escudero-Escribano, M.; Jaramillo, T. F. Core-Shell Au@Metal-Oxide Nanoparticle Electrocatalysts for Enhanced Oxygen Evolution. Nano Lett. **2017**, 17 (10), 6040–6046.

(5)   Carrasco, J. A.; Harvey, A.; Hanlon, D.; Lloret, V.; McAteer, D.; Sanchis-Gual, R.; Hirsch, A.; Hauke, F.; Abellán, G.; Coleman, J. N.; et al. Liquid Phase Exfoliation of Carbonate-Intercalated Layered Double Hydroxides. Chem. Commun. **2019**, 55 (23), 3315–3318.

(6)   Song, F.; Hu, X. Exfoliation of Layered Double Hydroxides for Enhanced Oxygen Evolution Catalysis. Nat. Commun. **2014**, 5, 4477.

(7)   Fang, Y.; Li, X.; Hu, Y.; Li, F.; Lin, X.; Tian, M.; An, X.; Fu, Y.; Jin, J.; Ma, J. Ultrasonication-Assisted Ultrafast Preparation of Multiwalled Carbon Nanotubes/Au/Co_3O_4 Tubular Hybrids as Superior Anode Materials for Oxygen Evolution Reaction. J. Power Sources **2015**, 300, 285–293.

(8)   Yu, Z. Y.; Duan, Y.; Liu, J. D.; Chen, Y.; Liu, X. K.; Liu, W.; Ma, T.; Li, Y.; Zheng, X. S.; Yao, T.; et al. Unconventional CN Vacancies Suppress Iron-Leaching in Prussian Blue Analogue Pre-Catalyst for Boosted Oxygen Evolution Catalysis. Nat. Commun. **2019**, 10 (1), 2799.

(9)   Cheng, H.; Su, C. Y.; Tan, Z. Y.; Tai, S. Z.; Liu, Z. Q. Interacting $ZnCo_2O_4$ and Au Nanodots on Carbon Nanotubes as Highly Efficient Water Oxidation Electrocatalyst. J. Power Sources 2017, 357, 1–10.

(10) Zhang, G.; Li, Y.; Zhou, Y.; Yang, F. NiFe Layered-double-hydroxide-derived $NiO-NiFe_2O_4$/Reduced Graphene Oxide Architectures for Enhanced Electrocatalysis of Alkaline Water Splitting. ChemElectroChem **2016**, 3 (11), 1927–1936.

(11) Chuang, C.-H.; Hsiao, L.-Y.; Yeh, M.-H.; Wang, Y.-C.; Chang, S.-C.; Tsai, L.-D.; Ho, K.-C. Prussian Blue Analogue-Derived Metal Oxides as Electrocatalysts for Oxygen Evolution Reaction: Tailoring the Molar Ratio of Cobalt to Iron. ACS Appl. Energy Mater. **2020**, 3 (12), 11752–11762.

(12) Han, L.; Tang, P.; Reyes-Carmona, Á.; Rodríguez-García, B.; Torréns, M.; Morante, J. R.; Arbiol, J.; Galan-Mascaros, J. R. Enhanced Activity and Acid PH Stability of Prussian Blue-Type Oxygen Evolution Electrocatalysts Processed by Chemical Etching. J. Am. Chem. Soc. **2016**, 138 (49), 16037–16045.

(13) Zhang, J.; Liu, J.; Xi, L.; Yu, Y.; Chen, N.; Sun, S.; Wang, W.; Lange, K. M.; Zhang, B. Single-Atom Au/NiFe Layered Double Hydroxide Electrocatalyst: Probing the Origin of Activity for Oxygen Evolution Reaction. J. Am. Chem. Soc. **2018**, 140 (11), 3876–3879.

(14) Zhang, Z.; Li, X.; Zhong, C.; Zhao, N.; Deng, Y.; Han, X.; Hu, W. Spontaneous

Synthesis of Silver-Nanoparticle-Decorated Transition-Metal Hydroxides for Enhanced

Oxygen Evolution Reaction. Angew. Chem. Int. Ed. **2020**, 59 (18), 7245–7250.